



# Modeling and Control of Aerial Robots

Robert Mahony, Randal W. Beard, Vijay Kumar

Aerial robotic vehicles are becoming a core field in mobile robotics. This chapter considers some of the fundamental modelling and control architectures in the most common aerial robotic platforms; small-scale rotor vehicles such as the quadrotor, hexacopter, or helicopter, and fixed wing vehicles. In order to control such vehicles one must begin with a good but sufficiently simple dynamic model. Based on such models, physically motivated control architectures can be developed. Such algorithms require realisable target trajectories along with real-time estimates of the system state obtained from on-board sensor suite. This chapter provides a first introduction across all these subjects for the quadrotor and fixed wing aerial robotic vehicles.

|   |      |
|---|------|
| 52.1 Overview .....                               | 1307 |
| 52.2 Modeling Aerial Robotic Vehicles .....       | 1309 |
| 52.2.1 Rigid Body Motion<br>of the Airframe ..... | 1309 |

|   |      |
|---|------|
| 52.2.2 Modeling for Quadrotors .....                        | 1310 |
| 52.2.3 Modeling<br>of Fixed-Wing Airplanes .....            | 1312 |
| 52.3 Control .....  | 1316 |
| 52.3.1 Quadrotor Control .....                              | 1316 |
| 52.3.2 Control<br>of Fixed-Wing Aircraft .....              | 1319 |
| 52.4 Trajectory Planning .....                              | 1324 |
| 52.4.1 Trajectory Planning<br>for Quadrotors .....          | 1324 |
| 52.4.2 Trajectory Planning<br>for Fixed-Wing Aircraft ..... | 1325 |
| 52.5 Estimating the Vehicle State .....                     | 1328 |
| 52.5.1 Estimating Attitude .....                            | 1328 |
| 52.5.2 Estimating Velocity<br>and Position .....            | 1329 |
| 52.6 Conclusion .....                                       | 1330 |
| Video-References .....                                      | 1331 |
| References .....  | 1331 |

## 52.1 Overview

The term *aerial robotics* is often attributed to *Robert Michelson* [52.1], as a term to capture a new class of autonomous and intelligent small flying machines. The quest for autonomy of aerial vehicles goes back almost to the origins of powered flight. The first autopilot for a fixed wing vehicle (the Sperry autopilot) was demonstrated in 1912, only a decade after the first powered flight by the Wright brothers. As early as World War I, the potential for an autonomously stabilized and remotely controlled airplane to be an effective weapon was understood and the Curtis-Sperry flying bomb first demonstrated autonomous unmanned flight in 1918 [52.2]. Autopilot technology was perfected during the 1930s as improving aircraft technology lead

to longer flight times and the need to relieve the pilot from constant attention to flight stability of the vehicle. Autonomous and radio controlled target aircraft were developed in the late 1930s and were extensively used during World War II for training. The German V-1 cruise missile, commonly known as the buzz bomb or doodlebug, was a highly successful autonomous vehicle; its relatively low impact in World War II being due to more British intelligence efforts than to the vehicles capabilities.

Following the World War II, the relative maturity of autopilot technology and airplane construction meant that the construction of unmanned fixed-wing vehicles was straightforward. Remote-controlled heli-

copters, such as the Gyrodyne QH-50 DASH, were developed as early as the 1960s. The Yamaha R-50 and subsequent Yamaha R-Max (Fig. 52.1), was developed during the 1980s and provides a remote controlled commercial aerial platform, with significant onboard autonomy, used primarily for agricultural applications.

Extensive development of fixed-wing autonomous vehicles was held back in the mid-20th century by the difficulty of localizing a vehicle when far from the base station. Indeed, the requirements of navigation systems for cruise missiles developed during the cold war was one of the main drivers for the development of satellite global positioning system (GPS) technology. Full operational capability of the United States GPS system with 24 satellites was declared in April 1995 and it was mandated as a dual-use system (both commercial and military) in 1996. Smaller scale commercial unmanned aerial vehicles were also constrained by the lack of robust and small-scale avionics systems. The availability of small low power computers, the development of microelectromechanical systems (MEMS) that provide affordable and robust Inertial Measurement Units (IMUs), and access to reliable GPS, lead to the beginning of the modern era of nonmilitary UAV and aerial robotic systems in the mid-1990s.

The largest class of commercial and military robotic aerial vehicles fly predominantly in obstacle free airspace. For such vehicles, once the aircraft has taken off, there is no need to employ obstacle avoidance techniques or interact with cluttered three-dimensional environments.

#### Definition 52.1

An *unmanned aerial vehicle* (UAV) is a system capable of sustained flight with no direct human control and able to perform a specific task.



**Fig. 52.1** Autonomous aerial robotic vehicle based on the Yamaha RMAX platform developed in the University of New South Wales, Australia (after [52.3, 4])

Navigation and control of an unmanned aerial vehicle is typically based on stabilizing a reference heading and altitude derived from the error between preset GPS way-points and the present vehicle position using a classical autopilot control system. The sensor suite used for control and navigation is usually a GPS and IMU along with barometric pressure. These sensor suites can be thought of as *proprioceptive* sensors, since they measure the internal state of the vehicle without reference to the external world. The kinds of tasks that UAVs are ideal for include high level surveillance and sensing tasks where the payload sensing suite is separate from the vehicle systems, with applications in agriculture, environmental monitoring, geophysical surveys, search and rescue, and security surveillance, as well as deployment of materials, where once again the payload is separate from the vehicle system, with applications in agriculture, search and rescue, and of course military missions. Such systems are a natural development of traditional flight technology and much of the research and development that goes into these vehicles is undertaken in aerospace departments in universities and aerospace companies.

#### Definition 52.2

An *aerial robotic vehicle* is an aerial vehicle capable of autonomously interacting with a complex dynamic three-dimensional environment and achieving complex environment-dependent goals.

The nature of the interaction with the environment for an aerial robotic vehicle, means that the presence of *exteroceptive* sensors, those that sense the environment around the vehicle, and how these sensor inputs are integrated into the vehicle guidance is the defining property of such a vehicle. Typical examples of exteroceptive sensors for aerial robotic vehicles are vision systems, laser range finders, acoustic sensors, etc., and external sensor systems such as VICON [52.5] and Optitrack [52.6] systems. The close coupling between the goal of the vehicle, its sensing suite, and the dynamic nature of the environment makes the simple way-point navigation control architecture of an unmanned aerial vehicle unsuitable for aerial robotic vehicles. The kinds of tasks that aerial robotic vehicles are ideal for are small-scale interactive tasks such as inspection of civil infrastructure including dam walls, girders of bridges, industrial pressure vessels; and surveillance tasks such as, inspection of damaged or burning buildings, monitoring of crowds, etc. Future applications may involve aerial manipulation including repair of infrastructure, and material handling in the construction and agricultural industries. Although the flight technology remains important, the sensing and control tasks become cru-

cial in such applications and the development that goes into these vehicles tends to be undertaken in robotics departments in universities and in the growing field of new aerial-robotics start-up companies. The ability to move in three-dimensional space brings new research challenges to the robotics community compared to the wheeled mobile robot technology that has motivated mobile robotics research over the last couple of decades.

## 52.2 Modeling Aerial Robotic Vehicles

There is already a vast range of aerial vehicle and UAV designs in existence, and there are even more ideas under development by companies and research groups as we write. In one short chapter, we must limit the scope of our presentation to a couple of the key examples. There are two major categories of vehicles that are used as platforms for aerial robotics: small-scale rotor vehicles such as the quadrotor, hexacopter, or helicopter, and fixed wing vehicles. The word *quad* is derived from the Latin *quadrangulum* for a four-sided figure. *Rotor* is derived from the Latin *rotationem* for a rotating object. However, *hexa* is derived directly from Greek for six. *Heli* is derived from ancient Greek *helikos* for spiral, while the term *copter* is derived from the modern term *helicopter*, a combination of *helikos* with the ancient Greek *pteron* for wing. Based on this etymology, we propose the terms *quadrotor* and *hexacopter* to describe the most common modern rotary wing aerial robotic vehicles in preference to the etymological questionable terms quadcopter and hexarotor that are also in common usage in the literature. We will present modeling and control material relevant to these two categories, focusing on the basic structure of the model. We will also focus on vehicles in 500 g–4 kg weight range as this corresponds to the primary general robotics applications where avionics and sensor suites take up the majority of the payload. Other classes of autonomous aerial vehicles that we are unable to cover in this chapter include lighter-than-air vehicles such as blimps and balloons, flapping wing vehicles, ducted fans, and rockets.

### 52.2.1 Rigid Body Motion of the Airframe

Heavier-than-air aerial robotic vehicles consist of a rigid airframe coupled with aerodynamic mechanisms to generate lift and thrust. For vehicles in the weight range considered, the compactness and structural integrity of the airframe means that there is little flexing of the airframe in normal operation and the rigid-body assumption is an effective model. In this case, the ve-

The term *unmanned aerial system* (UAS) is useful to refer to the combination of the infrastructure, human interfaces, aerial platform, and sensing and control subsystems. It is clear that certain vehicles may spend time operating in either UAV mode or aerial robotic mode and the terms are more useful to describe the way of thinking about the operation of a system rather than classifying a vehicle.

hicle model can be developed based on rigid-body dynamics with exogenous forces and torque generated by an aerodynamic model.

Let  $\{e_1, e_2, e_3\}$  be the coordinate axis unit vectors  $e_1 = (1, 0, 0)^T$ ,  $e_2 = (0, 1, 0)^T$ , and  $e_3 = (0, 0, 1)^T$  without specification of a frame of reference. Let  $\{B\}$  be a (right-hand) body fixed frame for the airframe with unit vectors  $\{b_1, b_2, b_3\}$  where these vectors are the axes of frame  $\{B\}$  with respect to frame  $\{A\}$  as shown in Fig. 52.2. Note that the convention for choice of axes shown in Fig. 52.2 is the convention common in the aerial robotics community [52.7–14], but is opposite to the usual convention in the aerospace community where the  $b_2$  and  $b_3$  axes are usually reversed in order so that  $b_3$  points down in the direction of gravity. In this chapter, we have chosen to follow the robotic community convention and this will lead to some nonconventional definitions for the modeling of fixed-wing airplanes. We will discuss this further in the specific sections on fixed-wing airplane modeling and control.

The orientation of the rigid body is given by a rotation matrix  ${}^A R_B = R = [b_1, b_2, b_3] \in \text{SO}(3)$  in the spe-

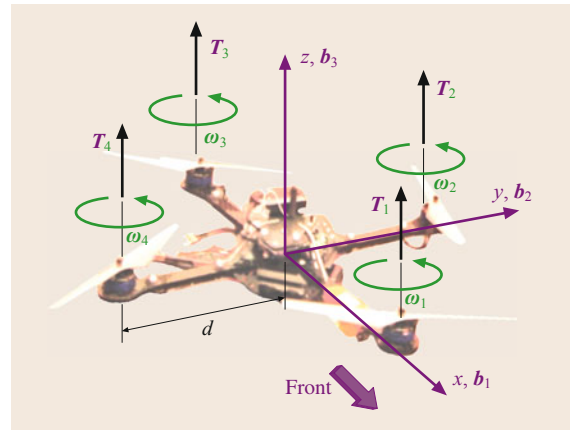


Fig. 52.2 The body-fixed frame and the directions of rotation for the propellers

cial orthogonal group. We have  $\mathbf{b}_1 = R\mathbf{e}_1$ ,  $\mathbf{b}_2 = R\mathbf{e}_2$ ,  $\mathbf{b}_3 = R\mathbf{e}_3$  by construction.

We will use Z-X-Y Euler angles to model this rotation as shown in Fig. 52.3. Note that this is not the normal roll-pitch-yaw convention used in aerospace. To get from  $\{A\}$  to  $\{B\}$ , we first rotate about  $\mathbf{e}_3$  by the yaw angle,  $\psi$ , and we will call this intermediary frame  $\{D\}$  with a basis  $\{\mathbf{d}_1, \mathbf{d}_2, \mathbf{d}_3\}$  where  $\mathbf{d}_i$  is expressed with respect to frame  $\{A\}$ . This is followed by a rotation about the  $x$ -axis in the rotated frame through the roll angle,  $\phi$ , to intermediary frame  $\{E\}$ , followed by a third pitch rotation about the new  $y$ -axis through the pitch angle  $\theta$  which results in the body-fixed triad  $\{\mathbf{b}_1, \mathbf{b}_2, \mathbf{b}_3\}$ . The associated rotation matrix is

$$R = \begin{pmatrix} c_\psi c_\theta - s_\phi s_\psi s_\theta & -c_\phi s_\psi & c_\psi s_\theta + c_\phi s_\phi s_\psi \\ c_\phi s_\psi + c_\psi s_\phi s_\theta & c_\phi c_\psi & s_\psi s_\theta - c_\phi c_\theta s_\phi \\ -c_\phi s_\theta & s_\phi & c_\phi c_\theta \end{pmatrix}. \quad (52.1)$$

where  $c$  and  $s$  are shorthand for cosine and sine, respectively.

Let  $\xi$  denote the position of the center of mass of the airframe in frame  $\{A\}$  and assume that this is also the origin of frame  $\{B\}$ . Let  $\mathbf{v} \in \{A\}$  denote the linear velocity of  $\{B\}$  with respect to  $\{A\}$  expressed in  $\{A\}$ . Let  $\Omega \in \{B\}$  denote the angular velocity of  $\{B\}$  with respect to  $\{A\}$ , this time expressed in  $\{B\}$ . Let  $m$  denote the mass of the rigid object and  $\mathbf{I} \in \mathbb{R}^{3 \times 3}$  denote the constant inertia matrix (expressed in the body fixed frame  $\{B\}$ ). The rigid body equations of motion of the airframe are [52.15, 16]

$$\dot{\xi} = \mathbf{v}, \quad (52.2a)$$

$$m\dot{\mathbf{v}} = -m\mathbf{g}\mathbf{e}_3 + R\mathbf{F}, \quad (52.2b)$$

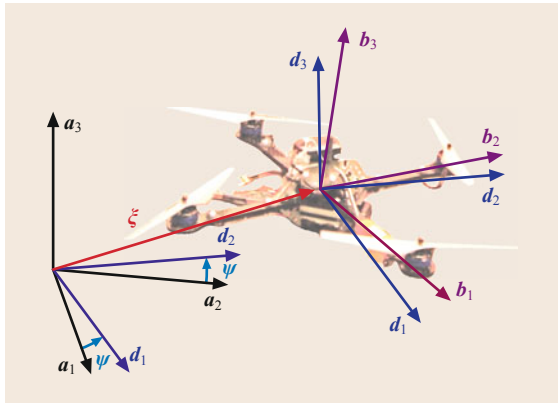


**Fig. 52.3** The vehicle model. The position and orientation of the robot in the global frame are denoted by  $\xi$  and  $R$ , respectively

$$\dot{R} = R\Omega_\times, \quad (52.2c)$$

$$\mathbf{I}\dot{\Omega} = -\Omega \times \mathbf{I}\Omega + \tau. \quad (52.2d)$$

The notation  $\Omega_\times$  denotes the skew-symmetric matrix such that  $\Omega_\times v = \Omega \times v$  for the vector cross-product  $\times$  and any vector  $v \in \mathbb{R}^3$ . The vectors  $\mathbf{F}, \tau \in \{B\}$  combine the principal nonconservative forces and torques applied to the airframe by the aerodynamics of the propulsion systems and lifting surfaces of the vehicle.

### 52.2.2 Modeling for Quadrotors

Quadrotors are currently the most popular research aerial robotics research platform because they are highly maneuverable and enable safe and low-cost experimentation in mapping, navigation, and control strategies in three dimensions. They are also arguably the simplest of the aerial robotics platforms to model for robotics applications. Early work in aerial robotics modeling and control dates back to the late 1990s and the field has remained active since [52.15–21].

In its most common form, the quadrotor vehicle is a very simple machine. It consists of four individual rotors attached to a rigid cross airframe as shown in Fig. 52.4. Control of a quadrotor is achieved by differential control of the thrust generated by each rotor. Pitch, roll, and heave (total thrust) control is straightforward to conceptualize. As shown in Fig. 52.2, rotor  $i$  rotates anticlockwise (positive about the  $z$ -axis) if  $i$  is even and clockwise if  $i$  is odd. Yaw control is obtained by adjusting the average speed of the clockwise and anticlockwise rotating rotors. The system is under-actuated and the remaining degrees of freedom corresponding to the translational velocity in the  $\mathbf{b}_1$ – $\mathbf{b}_2$  plane, must be controlled through the system dynamics.

The aerodynamics of rotors was extensively studied during the mid, 1900s with the development of manned helicopters and detailed models of rotor aerodynamics

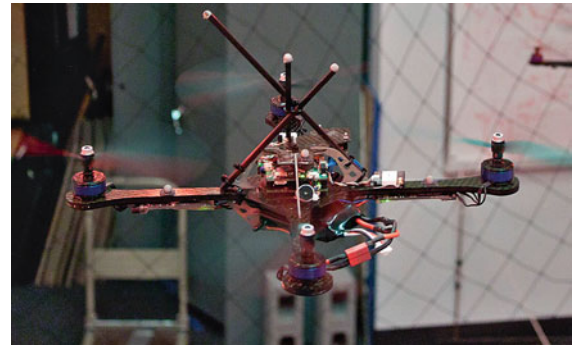


**Fig. 52.4** A quadrotor made by Ascending Technologies at the University of Pennsylvania with Vicon markers for state estimation

are available in the literature [52.22, 23]. Much of the detail in these aerodynamic models is useful for the design of rotor systems where the whole range of parameters (rotor geometry, profile, hinge mechanism, and much more) are fundamental to the design problem. For a typical robotic quadrotor vehicle, the rotor design is a question of choosing one among the several available rotors from the hobby shop and most of the complexity of aerodynamic modeling is best ignored. Nevertheless, a basic level of aerodynamic theory is important to understand the particularities of the control design.

The steady-state thrust generated by a hovering rotor (i.e., a rotor that is not translating horizontally or vertically) in free air may be modeled [52.23, Sect. 2.26] as

$$T_i := C_T \rho A_{r_i} r_i^2 \varpi_i^2, \quad (52.3)$$

where for rotor  $i$ ,  $A_{r_i}$  is the rotor disk area,  $r_i$  is the radius,  $\varpi_i$  is the angular velocity,  $C_T$  is the thrust coefficient that depends on rotor geometry and profile, and  $\rho$  is the density of air. In practice, a simple lumped parameter model

$$T_i = c_T \varpi_i^2, \quad (52.4)$$

is used where  $c_T > 0$  is modeled as a constant that can be easily determined from static thrust tests.

The reaction torque (due to rotor drag) acting on the airframe generated by a hovering rotor in free air may be modeled as [52.23, Sect. 2.30]

$$Q_i := c_Q \varpi_i^2, \quad (52.5)$$

where the coefficient  $c_Q$  (which also depends on  $A_{r_i}$ ,  $r_i$ , and  $\rho$ ) can be determined by static thrust tests.

As a first approximation, assume that each rotor thrust is oriented in the  $\mathbf{b}_3$ -axis of the vehicle, although we note that this assumption does not hold exactly for a rotor translating through the air.

The total thrust at hover  $T$  applied to the airframe is the sum of the thrusts from each individual rotor (Fig. 52.2)

$$T = \sum_{i=1}^4 |T_i| = c_T \left( \sum_{i=1}^4 \varpi_i^2 \right). \quad (52.6)$$

The hover thrust is the primary component of the exogenous force

$$F = Te_3 + \Delta \quad (52.7)$$

in (52.2b) where  $\Delta$  comprises secondary aerodynamic forces that are induced when the assumption that the rotor is in hover is violated.

The net moment arising from the aerodynamics (the combination of the individual rotor forces) applied to the quadrotor vehicle in directions  $\mathbf{b}_1$ ,  $\mathbf{b}_2$ , and  $\mathbf{b}_3$ , respectively, are

$$\begin{aligned} \tau_1 &= c_T d (\varpi_2^2 - \varpi_4^2), \\ \tau_2 &= -c_T d (\varpi_1^2 - \varpi_3^2), \\ \tau_3 &= c_Q \sum_{i=1}^4 \sigma_i \varpi_i^2, \end{aligned} \quad (52.8)$$

where  $d$  is the arm length of the quadrotor. A consequence of the structure of the thrust generation and the lack of aerodynamic lifting surfaces for a quadrotor means that one can solve for the heave and torque in a single equation in terms of the motor inputs

$$\underbrace{\begin{pmatrix} T \\ \tau_1 \\ \tau_2 \\ \tau_3 \end{pmatrix}}_F = \underbrace{\begin{pmatrix} c_T & c_T & c_T & c_T \\ 0 & dc_T & 0 & -dc_T \\ -dc_T & 0 & dc_T & 0 \\ -c_Q & c_Q & -c_Q & c_Q \end{pmatrix}}_G \begin{pmatrix} \varpi_1^2 \\ \varpi_2^2 \\ \varpi_3^2 \\ \varpi_4^2 \end{pmatrix}. \quad (52.9)$$

Inverting this relationship provides a mapping from desired control input for the rigid-body dynamics to rotor speed set-points for the motor control.

In practice, there are additional second-order aerodynamic effects present in the thrust generation for quadrotor vehicles [52.17, 19–21]. The principle second-order aerodynamic effects that are present at low speeds are *inflow variation*, *rotor flapping*, and *induced drag*. The first of these effects reduces the heave thrust when the quadrotor is ascending and increases the thrust when it is descending due to variation in rotor inflow velocity caused by the quadrotor motion. This acts as a damping term in the vertical direction of motion for the quadrotor. The remaining two effects generate forces that oppose horizontal translation of the quadrotor; blade flapping by inclining the rotor plane of flexible blade rotors and tilting the thrust vector away from the direction of motion, and induced drag by increasing the drag on the blade of a rigid rotor advancing in the direction of motion of the quadrotor [52.21]. In practice, it is difficult to separate the difference between the various effects and it is sufficient to model them all by a single damping force

$$\Delta = -Dv, \quad (52.10)$$

where  $D$  is a diagonally dominant positive definite matrix. For small quadrotors with relatively rigid rotor blades designed for hover performance, that is with



close to ideal chord and ideal twist, these effects are far more significant than is usual in classical helicopters and the effect must be modeled to achieve good control performance. These aerodynamic effects are also important in providing key low-frequency excitation to attitude and velocity estimation in the absence of GPS [52.21, 24–26].

At higher translation speeds, a quadrotor also experiences *translational lift*, *translational drag*, and *parasitic drag*. These aerodynamic effects are associated with efficiency gains in the rotor operation associated with increased inflow velocity generated by the forward velocity of the vehicle. Such effects are extremely important in large scale manned helicopters, which spend much of their time in forward flight. For many robotics applications, however, the vehicle is in quasi-stationary or near hover flight almost all the time and these secondary aerodynamic effects may be ignored. We will not discuss them further in this chapter but refer the interested reader to recent work [52.18, 20] and any of the classical helicopter texts [52.22, 23, 27].

### 52.2.3 Modeling of Fixed-Wing Airplanes

The conventional model for fixed-wing airplane uses a north-east-down frame of reference. The frame of reference used in this chapter, corresponding to the common aerial robotics convention inherited from the mobile-robotics community, is a north-west-up convention. We will still need to define the usual auxiliary angles associated with fixed-wing modeling and control, in particular; the angle-of-attack, side-slip, aerodynamic-bank, flight-path, and course angles. We will use the normal conventions to define these angles. The north-west-up convention now means that flight-path angle is positive when descending and negative when ascending, and positive roll leads course angle to decrease. The careful reader can easily transform between the conventions used here and the conventional airplane modeling approach and the authors apologize for any confusion that is caused by using a single convention for the whole chapter.

The key difference in modeling fixed-wing airplanes to quadrotors is that they rely on lift generated by airflow over the wings to support them in flight. The angle of incidence of the wind on the wing is a key variable in the dynamics of the vehicle and must be modeled in the dynamics. Since the main lift force is generated by an aerodynamic process, rather than directly by a controlled input as was the case for quadrotors and blimps, the modeling and control of an airplane is somewhat more complicated.

The aerodynamics of a fixed wing vehicle are defined relative to the local wind frame  $\{W\}$ . Frame  $\{W\}$

is chosen co-linear with the inertial frame  $\{A\}$ , but with linear velocity equal to the average extrinsic wind velocity with respect to the inertial frame. The wind frame is a Galilean frame (moving with constant velocity) with the property that it has zero extrinsic wind on average. Let  $v_a \in \{W\}$  denote the aerodynamic velocity of the vehicle, that is the linear velocity of the vehicle in the wind frame  $\{W\}$ . Let  $v_w \in \{A\}$  denote the average wind velocity as measured in the inertial frame  $\{A\}$ . Since the orientation of frames  $\{A\}$  and  $\{W\}$  are equal, the inertial velocity of the vehicle can be written as

$$v = v_a + v_w \in \{A\}.$$

To model the incident wind as seen by the vehicle as it flies through the air we introduce the flow frame (also termed the air frame) denoted by  $\{F\} = (f_1, f_2, f_3)$  where the orientation vectors  $\{f_i\}$  are expressed in the wind frame  $\{W\}$  which is co-linear with the inertial frame  $\{A\}$ . The first axis of the flow frame  $f_1$  is oriented in the direction of the incident wind on the vehicle,  $f_3$  is chosen to lie in the plane of symmetry of the vehicle orthogonal to  $b_2$ , and  $f_2$  makes up the right-hand frame. By construction, the velocity of the vehicle in the flow frame always lies in the direction  $f_1$ .

We define two orientation matrices associated with the wind frame. The angle-of-attack (AOA) matrix  ${}^B R_F = R_{\alpha, \beta}$  describes the orientation of the airflow frame  $\{F\}$  with respect to the body-fixed-frame  $\{B\}$  in terms of the *angle-of-attack*  $\alpha$ , and the *side-slip angle*  $\beta$  [52.28] (Fig. 52.5). Using the Z–Y–X Euler angle convention (yaw by  $\beta$ , pitch by  $\alpha$ , and there is no roll) we have

$$R_{\alpha, \beta} = \begin{pmatrix} c_\alpha c_\beta & -c_\alpha s_\beta & -s_\alpha \\ s_\beta & c_\beta & 0 \\ s_\alpha c_\beta & s_\alpha s_\beta & c_\alpha \end{pmatrix}. \quad (52.11)$$

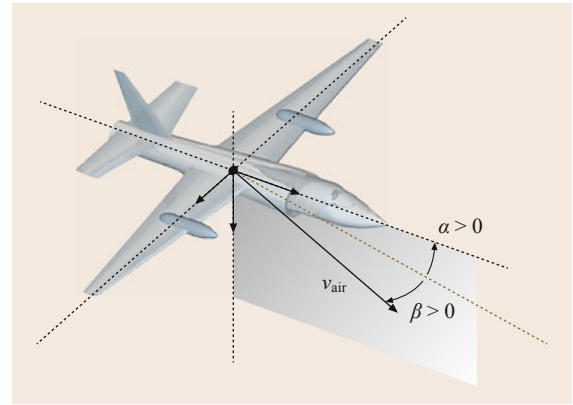


**Fig. 52.5** Representation of angle-of-attack, side-slip angle, and airspeed. Here  $v_{\text{air}}$  is denoted by  $v_a$  in the text to save space

The second orientation matrix is the flight-path matrix  ${}^W R_F = R_{\mu, \gamma, \chi}$  that denotes the orientation of the flow frame  $\{F\}$  with respect to the wind frame  $\{W\}$  in terms of the *aerodynamic bank angle*  $\mu$ , the *flight path angle*  $\gamma$ , and the *course angle*  $\chi$ . Using the Z-Y-X Euler angle convention (yaw by  $\chi$ , pitch by  $\gamma$ , and roll by  $\mu$ ) we have

$$R_{\mu, \gamma, \chi} = \begin{pmatrix} c_\gamma c_\chi & s_\gamma s_\mu c_\chi - c_\mu s_\chi & s_\gamma c_\mu c_\chi + s_\mu s_\chi \\ c_\gamma s_\chi & s_\gamma s_\mu s_\chi + c_\mu c_\chi & s_\gamma c_\mu s_\chi - s_\mu c_\chi \\ -s_\gamma & c_\gamma s_\mu & c_\gamma c_\mu \end{pmatrix}. \quad (52.12)$$

Note that the frames  $\{W\}$  and  $\{A\}$  are co-linear so  ${}^A R_F = {}^W R_F$ . It follows that  ${}^W R_F = {}^A R_F = {}^A R_B {}^B R_F$ .

Aerodynamic forces generated by lifting surfaces are proportional to the dynamic pressure [52.28]

$$\bar{Q} = \frac{1}{2} \rho |v_a|^2, \quad (52.13)$$

where  $\rho$  is the air density and  $|v_a|$  represents the air-speed or norm of the velocity  $v_a$ . Consider the situation where the aircraft is in normal flight, that is cruising at subsonic velocity while avoiding stall phenomenon. Let  $S$  denote the surface area of the wing (or lifting surface of the vehicle). The lift  $L = F_Z^a$  generated by the lifting surface is defined as the aerodynamic force oriented in the  $f_3$  direction in flow frame  $\{F\}$  and can be modeled as

$$L = \bar{Q} S C_L^\alpha (\alpha + \alpha_0) + \bar{Q} S C_L^\beta \beta \\ \approx \bar{Q} S (C_L + C_L^\alpha \alpha) \quad (52.14)$$

for sufficiently small angle of attack  $\alpha$  (typically less than  $15^\circ$ ). The terms  $C_L^\alpha (\alpha + \alpha_0)$  and  $C_L^\beta \beta$  are linear approximations to the lift-coefficient curves for small  $\alpha$  and  $\beta$  [52.28]. The offset angle of attack  $\alpha_0$  is thought of as the effective angle of attack of the wing in normal level flight conditions. In particular, at normal cruising speed in level flight,  $\bar{Q} S C_L^\alpha \alpha_0 = mg$  is the lift required to sustain the vehicle in level flight, so that  $\alpha, \beta = 0$  in level flight. The term  $\bar{Q} S C_L^\beta \beta$  is small and can be discarded in many applications.

The drag  $D = -F_X^a$  is a combination of parasitic and induced drag and is oriented in the  $-f_1$  direction.

$$D = \bar{Q} S [C_D^\rho + \kappa (C_L^\alpha)^2 (\alpha + \alpha_0)^2] \\ \approx \bar{Q} S (C_D + C_D^\alpha \alpha), \quad (52.15)$$

where  $\kappa$  is the *Oswald coefficient* [52.28] and the second equation is obtained by ignoring  $\alpha^2$  terms. The

constant  $C_D$  combines the parasitic drag coefficient  $C_D^\rho$  along with the induced drag  $\kappa (C_L^\alpha)^2 \alpha_0^2$  due to  $\alpha_0$ , while  $C_D = 2\kappa \alpha_0 (C_L^\alpha)^2$  is the linear coefficient for the dependence of induced drag on the angle-of-attack. It is also possible to model a contribution  $\bar{Q} S C_D^\beta \beta$  to the drag force, however, this is sufficiently small that it is normally ignored. There is a final lateral aerodynamic force component  $F_Y^a$  that is due to side-slip

$$F_Y^a = \bar{Q} S C_Y^\beta \beta. \quad (52.16)$$

The propeller or thrust mechanism of a fixed wing vehicle generates thrust  $T$  in direction  $b_x$  in the body-fixed-frame. The total linear force  $F \in \{B\}$  applied to the vehicle due to aerodynamic effects and thrust effects is

$$F = R_{\alpha, \beta} (F_X^a, F_Y^a, F_Z^a)^T + (T, 0, 0)^T \\ = \begin{pmatrix} T \\ 0 \\ 0 \end{pmatrix} + \bar{Q} S \begin{pmatrix} -C_D c_\alpha c_\beta - C_L s_\alpha \\ -C_D s_\beta \\ -C_D s_\alpha c_\beta + C_L c_\alpha \end{pmatrix} \\ + \bar{Q} S \begin{pmatrix} -C_D^\alpha c_\alpha c_\beta - C_L^\alpha s_\alpha \\ -C_D^\alpha s_\beta \\ -C_D^\alpha s_\alpha c_\beta + C_L^\alpha c_\alpha \end{pmatrix} \alpha \\ + \bar{Q} S \begin{pmatrix} -C_D^\beta c_\alpha c_\beta - C_Y^\beta c_\alpha s_\beta - C_L^\beta s_\alpha \\ -C_D^\beta s_\beta + C_Y^\beta c_\beta \\ -C_D^\beta s_\alpha c_\beta + C_Y^\beta s_\alpha s_\beta + C_L^\beta c_\alpha \end{pmatrix} \beta \quad (52.17)$$

expressed in the flow frame.

The aerodynamic moments  $\tau \in \{B\}$  in the body-fixed frame are modeled by

$$\begin{pmatrix} \tau^x \\ \tau^y \\ \tau^z \end{pmatrix} = \bar{Q} S l \begin{pmatrix} C_x^\beta \beta + C_x^\rho \frac{c \Omega_x}{2|v_a|} + C_x^r \frac{c \Omega_z}{2|v_a|} + C_x^\delta \delta_x \\ C_y + C_y^\alpha \alpha + C_y^q \frac{b \Omega_y}{2|v_a|} + C_y^\delta (\delta_y + \delta_y^0) \\ C_z^\beta \beta + C_z^r \frac{c \Omega_z}{2|v_a|} + C_z^\delta \delta_z \end{pmatrix}, \quad (52.18)$$

where  $(\Omega_x, \Omega_y, \Omega_z)$  are the components of the angular velocity  $\Omega \in \{B\}$  and represent the roll, pitch and yaw rates of body-fixed frame, respectively;  $b$  is the wing span,  $c$  is the mean cord of the wing,

and  $(\delta_x, \delta_y, \delta_z)$  are deflections of the airplane control surfaces (ailerons, elevator, and rudder). The constants  $\{C_x^p, C_x^r, C_x^\delta, C_y, C_y^\alpha, C_y^q, C_y^\delta, C_z^\beta, C_z^r, C_z^\delta\}$  are dimensionless aerodynamic coefficients [52.28]. In normal trim conditions, the trimmed elevator deflection  $\delta_y^0$  is chosen to cancel the static moment  $C_y$  generated by the wing in level flight,  $C_y^\delta \delta_y^0 = -C_y$ .

Combining (52.17) and (52.18) with (52.2) yields a dynamic model for a fixed wing vehicle with minimal approximations. The resulting equations of motion are complex and can be difficult to work with directly. The most common approach to control fixed-wing vehicles based on the full model is to take this model and linearize the state equations, either along a trajectory, or in regions of state space. The resulting model is either a linear time-varying or linear parameter varying system and can be controlled using classical linear system control techniques [52.29]. Although this approach is well established in the aerospace industry it tends to hide the underlying structure of the dynamics and requires good models of the various aerodynamic parameters, a challenge for many aerial robots with airframes that are always subject to being fiddled with and having sensor packages attached externally. For aerial robotic applications it is of interest to consider a simplified but still structurally consistent model of fixed wing dynamics and use robust and simple control strategies.

### Bank-to-Turn Flight Regime

In this section, we propose a model that is suitable for a wide range of fixed-wing applications where the vehicle is in normal flight mode. The approach taken uses a flight regime where the lateral acceleration required to turn the vehicle is obtained by tilting the lift generated by the wings, a strategy termed *bank-to-turn* or *coordinated turn* in the aerospace literature [52.30, 31]. A bank-to-turn maneuver is characterized by zero sideslip,  $\beta = 0$ , and leads to considerable simplification of the equations of motion. This is a very common mode of flying for any fixed-wing vehicle and, unless the task requires aerobatic maneuvers or the vehicle lacks control surface actuation, is the natural mode to control a UAV.

Given that accurate measurements of the roll rates  $\Omega$  are available through an onboard IMU system and most UAV systems have large control surfaces relative to their size, it is possible to use high gain to dominate the attitude dynamics (52.2d) and (52.18). That is, the angular velocity  $\Omega \approx \Omega^*$  can be thought of as an input to the reduced order model (52.2a), (52.2b), (52.2c). The above discussion motivates a dynamic reduction of the system equations with new inputs  $\Omega^*$ , as well as  $T$  the propeller thrust.

Based on the assumption that the vehicle is flying using bank-to-turn control and for small angle-of-attack then the approximation  $\beta \approx 0$  holds and simplified dynamic equations can be derived. Using this approximation and canceling all second-order terms in  $\alpha$  and  $\beta$  allows one to rewrite (52.17) as

$$F = \begin{pmatrix} T \\ 0 \\ 0 \end{pmatrix} + \bar{Q}S \begin{pmatrix} -C_D \\ 0 \\ C_L \end{pmatrix} + \bar{Q}S \begin{pmatrix} -C_D^\alpha - C_L \\ 0 \\ C_L^\alpha - C_D \end{pmatrix} \alpha. \quad (52.19)$$

From the construction of  $\{F\}$  we have  ${}^v F_a = |v_a|f_1$  by definition. It follows that (52.2a) can be written as

$$\dot{\xi} = v_a = |v_a|R_{\mu,\gamma,\chi}e_1.$$

Note that  $R_{\mu,\gamma,\chi}e_1 = (c_\chi c_\gamma, s_\chi c_\gamma, -s_\gamma)^T$  does not depend on the aerodynamic bank angle  $\mu$ . Thus,  $(|v_a|, \gamma, \chi)$  can be used as generalized coordinates for the velocity of the vehicle

$$\dot{\xi} = |v_a|(c_\chi c_\gamma, s_\chi c_\gamma, -s_\gamma)^T. \quad (52.20)$$

Differentiating  $v_a = \dot{\xi}$  and rearranging yields

$$\dot{v}_a = R_{\mu,\gamma,\chi} \begin{pmatrix} 1 & 0 & 0 \\ 0 & |v_a|c_\gamma s_\mu & -|v_a|s_\mu \\ 0 & -|v_a|c_\gamma s_\mu & -|v_a|c_\mu \end{pmatrix} \begin{pmatrix} \dot{|v_a|} \\ \dot{\gamma} \\ \dot{\chi} \end{pmatrix}. \quad (52.21)$$

Consider the (3, 2) element of (52.12) and recall that  $R_{\mu,\gamma,\chi} = R_{\phi,\theta,\psi}R_{\alpha,\beta}$  and applying  $\beta \equiv 0$  then  $s_\mu c_\gamma = s_\phi$  and we have

$$s_\mu = \frac{s_\phi}{c_\gamma} \quad (52.22)$$

for normal flight conditions where  $c_\gamma \neq 0$  and  $s_\phi < c_\gamma$ . By simple geometry,

$$c_\mu = \frac{1}{c_\gamma} \sqrt{c_\gamma^2 - s_\phi^2},$$

and the dependence on the bank angle can be removed entirely from kinematics of  $(|v_a|, \gamma, \chi)$  to be replaced by the roll angle  $\phi$ .



Inverting (52.21) and substituting for (52.2b), (52.19) and for (52.22) we obtain

$$\begin{aligned} \frac{d}{dt}|v_a| &= -gs_\gamma + \frac{T}{m}c_\alpha - \alpha \frac{\bar{Q}S}{m}(C_D^\alpha + C_L) \\ &\quad - \frac{\bar{Q}S}{m}C_D, \end{aligned} \quad (52.23a)$$

$$\dot{\chi} = -\frac{s_\phi}{c_\gamma} \left( \frac{\bar{Q}S}{mc_\gamma} C_L + (C_L^\alpha - C_D)\alpha \right), \quad (52.23b)$$

$$\begin{aligned} \dot{\gamma} &= \frac{gc_\gamma}{|v_a|} + \alpha \frac{\bar{Q}S}{m}(C_L^\alpha - C_D) \\ &\quad - C_L \frac{\bar{Q}S \sqrt{c_\gamma^2 - s_\phi^2}}{m|v_a|c_\gamma}, \end{aligned} \quad (52.23c)$$

where one should recall that  $\bar{Q} = \frac{1}{2}\rho|v_a|^2$  (52.13) depends on  $|v_a|$ .

Note that for  $\alpha$  small,  $T$  provides a free input to stabilize the speed of the vehicle in (52.23a), although we have seen in Sect. 52.3.2 that a different approach is advantageous in practice. In (52.23b), there is no direct input variable, however, the roll  $\phi$  will play this role in the control design. Similarly, in (52.23c), the angle-of-attack  $\alpha$ , which itself has dynamics, must be used to control  $\gamma$ . In fact, both (52.23b) and (52.23c) depend on a complex mix of variables including dynamic pressure (and consequently  $|v_a|$ ) as well as  $\phi$ ,  $\alpha$  and  $\gamma$ . Nevertheless, the identification of roll  $\phi$  with control of heading and angle-of-attack  $\alpha$  with control of flight path is a natural approach in the development of aircraft control.

The kinematics of  $\phi$  are straightforward to compute by differentiating (52.1). Differentiating the (3, 2) entry of  $R_{\phi,\theta,\psi}$  (52.1) we have

$$\dot{\phi} = \Omega_x c_\theta + \Omega_z s_\theta. \quad (52.24)$$

The primary control for  $\dot{\phi}$  is the roll angular velocity  $\Omega_x$  and this control will be used to cancel the disturbance created by  $\Omega_z$  as discussed in Sect. 52.3.2.

To model the dynamics of  $\alpha$ , recall the relationship  $R_{\mu,\gamma,\chi} = R_{\phi,\theta,\psi} R_{\alpha,\beta}$  again. This time considering the (3, 1) element of  $R_{\mu,\gamma,\chi}$  we obtain

$$\begin{aligned} \dot{\alpha} (c_\phi s_\theta s_\alpha + c_\alpha c_\phi c_\theta) &= \\ &= -s_\phi c_\alpha \Omega_x + s_\phi s_\alpha \Omega_z \\ &\quad + (c_\phi s_\theta s_\alpha + c_\phi c_\theta c_\alpha) \Omega_y \\ &\quad - c_\gamma \dot{\gamma}. \end{aligned} \quad (52.25)$$

Back substituting from (52.23c) and rearranging yields

$$\begin{aligned} \dot{\alpha} &= \Omega_y + \frac{s_\phi s_\alpha \Omega_z - s_\phi c_\alpha \Omega_x}{(c_\phi s_\theta s_\alpha + c_\alpha c_\phi c_\theta)} \\ &\quad - c_\gamma \left[ \frac{gc_\gamma}{|v_a|} + \alpha \frac{\bar{Q}S}{m}(C_L^\alpha - C_D) - \frac{\bar{Q}S c_\mu}{m|v_a|} C_L \right], \end{aligned} \quad (52.26)$$

where the denominators are always well defined for normal flight conditions. The angular velocity  $\Omega_y$  enters (52.26) as a free input providing the control for AOA.

Equations (52.23a), (52.23c) and (52.26) lead to a cascade nonlinear system

$$\dot{\chi} = -s_\phi \left( \frac{|v_a|^2}{c_\gamma^2} A_2 + \frac{\alpha}{c_\gamma} A_3 \right), \quad (52.27a)$$

$$\dot{\phi} = u_\phi, \quad (52.27b)$$

$$\dot{h} = -|v_a|s_\gamma, \quad (52.27c)$$

$$\frac{d}{dt}|v_a| = TA_1 - gs_\gamma + f_1(\gamma, \alpha, |v_a|), \quad (52.27d)$$

$$\begin{aligned} \dot{\gamma} &= \alpha |v_a|^2 A_4 - \frac{|v_a|}{c_\gamma} (c_\gamma^2 - s_\phi^2)^{\frac{1}{2}} A_5 \\ &\quad + f_2(\gamma, |v_a|), \end{aligned} \quad (52.27e)$$

$$\dot{\alpha} = u_\alpha + f_3(\gamma, \alpha, |v_a|; t), \quad (52.27f)$$

with the following constants

$$A_1 = \frac{c_\alpha}{m}, \quad A_2 = \frac{C_L \rho S}{2m}, \quad A_3 = (C_L^\alpha - C_D),$$

$$A_4 = \frac{\rho S}{2m}(C_L^\alpha - C_D), \quad A_5 = C_L \frac{\rho S}{2m},$$

functions;

$$f_1(\gamma, \alpha, |v_a|) = -\alpha \frac{\bar{Q}S}{m}(C_D^\alpha + C_L) - \frac{\bar{Q}S}{m}C_D,$$

$$f_2(\gamma, |v_a|) = \frac{gc_\gamma}{|v_a|},$$

$$\begin{aligned} f_3(\gamma, \alpha, |v_a|) &= -c_\gamma \left[ \frac{gc_\gamma}{|v_a|} + \alpha \frac{\bar{Q}S}{m}(C_L^\alpha - C_D) \right. \\ &\quad \left. - \frac{\bar{Q}S c_\mu}{m|v_a|} C_L \right], \end{aligned}$$

and the input functions;

$$u_\phi = \Omega_x c_\theta + \Omega_z s_\theta,$$

$$u_\alpha = \Omega_y + \frac{s_\phi s_\alpha \Omega_z - s_\phi c_\alpha \Omega_x}{(c_\phi s_\theta s_\alpha + c_\alpha c_\phi c_\theta)}.$$

Here the height  $h$  kinematics have been added to complete the bank-to-turn dynamics. The course (52.27a), and the height (52.27c) dynamics have negative signs compared to conventional fixed-wing modeling developments due to the nonstandard north-west-up convention chosen.

These equations are fully nonlinear equations based on the sliding mode simplification associated with holding  $\beta \equiv 0$ . The condition on side-slip angle will can be enforced using the free degree of freedom in  $\Omega_z$  as will be discussed in Sect. 52.3.2. We note that the dynamics presented in this section are closely related to the *longitudinal dynamics* considered in classical aeronau-

tical texts that treat the angle of attack, glide angle, and velocity of the vehicle. The more classical expressions for longitudinal control of a fixed-wing vehicle are obtained from the above model by setting  $\dot{\chi} = \mu = \phi = 0$ . An additional simplifying assumption often made for the course kinematics (52.27a) is that lift is compensating gravity during level-flight. With these assumptions, (52.27a) can be replaced by

$$\dot{\chi} = -\frac{g}{|v_a|} \tan(\phi)$$

based on centripetal force balance.

## 52.3 Control

Control for aerial vehicles is challenging for a number of reasons. First, most aerial vehicles are under actuated and the control design must exploit interactions between dynamic states to control the vehicle. Second, aerial vehicles use aerodynamic effects for thrust and lift generation, and regulation of these forces is by nature approximate, leading to significant modeling error. Third, external effects such as wind, turbulence, and vortex generation, lead to high levels of load disturbance in the control loops. Finally, it is often difficult or impossible to measure the vehicle and aerodynamic state directly making it necessary to use an observer or design the controller from first principles to use explicit measurements.

Most aerial vehicles are controlled using a hierarchical control structure with nested feedback loops based on three levels; planning, guidance, and control:

- **Planning:** It is the outermost loop in aerial vehicle control and is associated with path planning, setting way-points, etc.
- **Guidance:** The guidance level of control concerns tracking trajectories to achieve local goals. This control loop is typically designed using the attitude reference as a virtual input, leading to a fully actuated control problem.
- **Control:** It is the high gain innermost loop of the control hierarchy and is concerned primarily with attitude and flight stability of the vehicle. This control problem is typically fully actuated and can be tackled using standard control techniques.

The more dynamic and aggressive the task considered is, the more these levels of control will interact and an integrated control design must be considered. However, in most real-world situations, splitting the control into three hierarchical levels leads to a simpler design

problem that achieves the desired performance. For example, the recent aggressive maneuvers undertaken and demonstrated in quadrotor control are based on hierarchical control strategies that use trajectory planning processes for the outer loop that specify achievable trajectories that then are stabilized in real-time using attitude as a virtual input, with high-gain feedback on the inner-loop attitude stability control. Most of this work has been done with the use of external motion capture systems to provide the inertial frame position and velocity feedback [52.7–12, 32]. However, more recently there have been a few attempts to do this with on-board cameras and inertial measurement units [52.13, 14].

### 52.3.1 Quadrotor Control

The quadrotor control and guidance problem is conceptually more straightforward than that of fixed-wing vehicles. In its simplest form, the goal is to design control algorithms to track smooth feasible trajectories  $(R^*(t), \xi^*(t)) \in \text{SE}(3)$ . We will assume that a planner specifies the full desired trajectory, including the higher order derivative terms  $(\Omega^*(t), \dot{\xi}^*(t))$  and  $(\ddot{\Omega}^*(t), \ddot{\xi}^*(t))$ . A quadrotor vehicle is an under-actuated system – there are four inputs  $\mathbf{u} = (T, \tau^T)^T$ , while the trajectory lives in  $\text{SE}(3)$  and is six-dimensional. The hierarchical control structure proposed leads to an inner loop regulating the attitude using the moments  $\tau$  as the control input. The guidance level utilizes the attitude  $R$  and heave  $T$  to regulate the trajectory  $\xi(t)$  to track  $\xi^*(t)$ . In high performance control of a quadrotor, the major limitation to performance comes from the limits of motor response and the control hierarchy must be augmented by a low level motor regulation system. The proposed control architecture forms nested feedback loops as shown in Fig. 52.6.

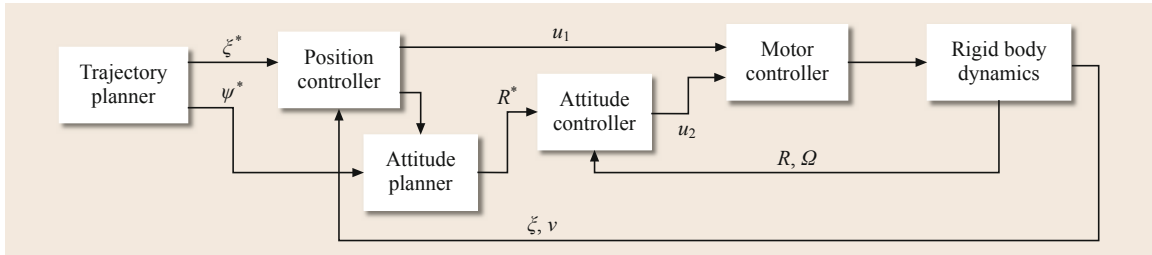


**Fig. 52.6** Typical control architecture. A base-level motor regulation, an inner attitude control loop, an intermediate position guidance loop, with an outer trajectory planner

### Motor Regulation

The aerodynamics of thrust generation by rotors is a subject that has been studied in detail in the classical rotorcraft literature [52.22, 23, 27]. Using a full model of rotor aerodynamics has significant potential in the design of the motor control for high-performance rotor control for aerial robotic applications [52.33]. Despite this, it is sufficient in most cases to consider a static thrust model that holds for a rotor in hover and is a reasonable approximation for most robotic applications. In such a model, the thrust generated is proportional to the square of the rotor speed. Since most quadrotor vehicles are equipped with brushless DC motors that use back EMF sensing for rotor commutation, making it possible to measure rotor angular velocity, the control of the rotor thrust is usually implemented as a local control loop on the electronic speed controller (ESC) regulating rotor speed.

Most ESC use PWM (pulse width modulation) regulation of voltage bus to provide voltage control of the motors. A typical rise time for the uncontrolled system is in the order of 200 ms and it is necessary to include a local control loop to improve the system response. The aerodynamic drag of the rotor means that the system is naturally heavily damped and there is no need for derivative control. Similarly, an integral term is rarely deemed necessary at the rotor control level since the thrust model used is not particularly accurate anyway and it will always be necessary to have integral control at higher levels in the control hierarchy. Since an integral term is inadvisable, it is important to use the best model of the thrust generation possible as a feedforward term  $V_{ff}(\varpi_i^*)$  to minimize the requirement on the proportional regulation. Thus, a typical ESC rotor control is given by saturated proportional control with feedforward [52.34]

$$V_i = \text{sat} [k(\varpi_i^* - \varpi_i) + V_{ff}(\varpi_i^*)], \quad (52.28)$$

where  $V_i$  is the applied motor voltage,  $\varpi_i^*$  is the desired speed and the actual motor speed  $\varpi_i$  is measured from the electronic commutation in the embedded

speed controller. The performance of the motor controllers is ultimately limited by the current that can be supplied from the batteries [52.34] and a saturation on the demanded voltage is necessary. Without the saturation, extreme maneuvers may cause the voltage bus to drop excessively, destroying the rotor regulation performance and unless care is taken, causing the onboard electronics to brownout.

### Attitude Control

The control problem considered in attitude regulation is to use full actuation of  $\tau$  in (52.2d) to control (52.2c) to track a desired attitude trajectory  $R^*(t)$  along with its velocity  $\Omega^*(t)$  such that  $\dot{R}^*(t) = R^*(t)\Omega^*(t)$ . The approach described uses a global stability design based on minimizing the matrix error

$$\tilde{R} = (R^*)^T R \quad (52.29)$$

similar to [52.7, 35]. Driving  $\tilde{R} \rightarrow I_3$  ensures that  $R \rightarrow R^*$ . The kinematics of the tracking error is given by

$$\begin{aligned} \dot{\tilde{R}} &= -\Omega_\times^* \tilde{R} + \tilde{R} \Omega_\times \\ &= [\tilde{R}, \Omega_\times^*] + \tilde{R}(\Omega_\times - \Omega_\times^*) \\ &= [\tilde{R}, \Omega_\times^*] + \tilde{R} \tilde{\Omega}_\times, \end{aligned} \quad (52.30)$$

where  $[A, B] = AB - BA$  is the matrix commutator and

$$\tilde{\Omega} := \Omega - \Omega^*. \quad (52.31)$$

We assume that derivative  $\dot{\Omega}^*$  of the target angular velocity is available for the purposes of designing a feedforward torque for the angular velocity dynamics

$$\tau^* := \mathbf{I} \dot{\Omega}^* + \Omega_\times^* \mathbf{I} \Omega^*, \quad (52.32)$$

where  $\mathbf{I}$  is the inertia matrix of the airframe (52.2d). Feed-forward control for the angular velocity of the attitude is important for high-performance maneuvers, especially when the motor response is pushed to near performance limits. The higher derivative information

for the angular velocity is available from path planning algorithms such as those discussed in Sect. 52.4.1 or using predictive control algorithms [52.8–10, 36]. Choose the control input

$$\tau := \tau^* + \mathbf{u}_2 \quad (52.33)$$

where  $\mathbf{u}_2 \in \mathbb{R}^3$  is the free control that will be used to stabilize the error dynamics (Fig. 52.6). The error dynamics for the angular velocity error are now

$$\mathbf{I}\dot{\tilde{\Omega}} = -\tilde{\Omega}_\times \mathbf{I}\tilde{\Omega} + \mathbf{u}_2. \quad (52.34)$$

The goal is to choose  $\mathbf{u}_2$  in order to stabilize the error dynamics (52.30) and (52.34) robustly. Define

$$\mathbb{P}(\tilde{R}) := \frac{1}{2}(\tilde{R} - \tilde{R}^T)$$

to be the skew-symmetric projection of the error matrix. It can be verified that  $\mathbb{P}(\tilde{R}) = \sin(\theta)a_\times$  where  $(a, \theta)$  is the angle-axis representation of  $\tilde{R}$ . That is the skew-symmetric projection is the axis of rotation that rotates  $R$  to  $R^*$  (equivalently rotates  $\tilde{R}$  to the identity) scaled by the sin of the angle between the two orientations. Choose a proportional–derivative (PD) control

$$\mathbf{u}_2 = -k_P \text{vex}(\mathbb{P}(\tilde{R})) - k_D \tilde{\Omega},$$

where  $\text{vex}: \mathbb{R}^{3 \times 3} \rightarrow \mathbb{R}^3$  is the inverse of the skew-symmetric operator applied to skew-symmetric matrices,  $\text{vex}(\Omega_\times) = \Omega$ . The proportional term applies a torque associated with a nonlinear spring associated with a potential energy  $\text{tr}(\tilde{R}^T \tilde{R})$  while the derivative  $k_D \tilde{\Omega}$  provides damping. It is straightforward to demonstrate that the Lyapunov function

$$\mathcal{L} := k_P \text{tr}(\tilde{R}^T \tilde{R}) + \frac{1}{2} \tilde{\Omega}^T \mathbf{I} \tilde{\Omega}$$

is decreasing

$$\frac{d}{dt} \mathcal{L} := -k_D \|\tilde{\Omega}\|^2.$$

Invoking Barbalat's lemma, with some care, it follows that the system is almost globally asymptotically stable. The zero measure exception set for the basin of attraction is associated with situations where the quadrotor is completely flipped,  $\theta = \pi$  rad, and  $\mathbb{P}(\tilde{R}) = 0$  even though  $\tilde{R} \neq I$ .

To verify the local exponential convergence and provide guidance for the gain tuning, we consider the linearization of (52.30) and (52.34). Write  $\tilde{R} \approx I + (z_R)_\times$  where the skew-symmetric matrix  $(z_R)_\times$  (for  $z_R \in$

$\mathbb{R}^3$ ) is the linear approximation of  $\tilde{R}$  around the identity matrix  $I$ . Write  $\tilde{\Omega} \approx z_\Omega$  for the linear approximation of  $\tilde{\Omega}$  around the origin  $\tilde{\Omega} = 0$ . The linearization of the error  $z = (z_R, z_\Omega)$  system is given by

$$\begin{pmatrix} \dot{z}_R \\ \dot{z}_\Omega \end{pmatrix} = \begin{bmatrix} ((\Omega^*)_\times & 0 \\ 0 & \mathbf{I}^{-1}(\mathbf{I}\Omega)_\times \end{bmatrix} + \begin{pmatrix} 0 & 1 \\ -k_P \mathbf{I}^{-1} & -k_D \mathbf{I}^{-1} \end{pmatrix} \begin{pmatrix} z_R \\ z_\Omega \end{pmatrix} \quad (52.35)$$

or in more compact notation  $\dot{z} = A(t)z$  where  $A(t) = A_1(t) + A_2$  comprises the sum of two matrices in (52.35). The matrix  $A_1(t)$  is a time-varying matrix depending on the exogenous system signals  $\Omega$  and  $\Omega^*$  while the second matrix  $A_2$  is a time-invariant Hurwitz second-order linear system matrix. It is straightforward to show that this system is asymptotically stable using a Lyapunov function  $\ell = k_P/2|z_R|^2 + 1/2z_\Omega^T \mathbf{I} z_\Omega$ , using an analog of the nonlinear argument made earlier. We have that  $\dot{\ell} = -k_D|z_\Omega|^2$ . Define  $C = \begin{pmatrix} 0 & I_3 \end{pmatrix} \in \mathbb{R}^{3 \times 6}$  then if the pair  $(A(t), C)$  is uniformly completely observable (UCO) asymptotic stability implies exponential stability [52.37, pp. 626–628]. It is intuitively clear that the system matrices  $(A(t), C)$  associated with (52.35) are UCO, although providing the algebraic proof is beyond the scope of this chapter. Tuning the gains is then a process of choosing  $k_P$  and  $k_D$  to assign the eigenvalues of the Hurwitz system matrix, with an eye to dominate the oscillatory, but bounded energy, disturbance introduced by  $A_1(t)$ .

### Trajectory Tracking Control

The trajectory planning algorithm, discussed later in Sect. 52.4.1, provides a full trajectory specification as well as the feedforward inputs consisting of  $(\xi^p, \dot{\xi}^p, R^p, \Omega^p, \dot{\Omega}^p, u_1^p, u_2^p)$  and their derivatives. The goal of trajectory tracking control is to regulate the linear dynamics of a quadrotor to track a specified goal trajectory  $\xi^*(t)$ . Trajectory tracking control operates at a higher level in the hierarchy of the quadrotor control architecture (Fig. 52.6) and the desired attitude  $R^*$  used in the attitude control loop is designed as an input in the trajectory loop control design. In addition to specifying the attitude goal,  $R^*$ , the trajectory tracking control specifies the heave (total thrust),  $T$ , input reference that is used along with (52.33) for the low-level motor control reference (52.9).

The linear trajectory goal  $\xi^* = \xi^p$  and  $\dot{\xi}^* = \dot{\xi}^p$  are used directly from the path planning design as the goal of the trajectory planner. The actuation for the linear dynamics, however, depends on the attitude of the vehicle. Thus, it is necessary to define the goal for the attitude control  $R^*$  as a part of the control design

rather than rely on the planned trajectory set-point; in particular  $R^* \neq R^p$  in general. Note that the feedforward control in Sect. 52.3.1 requires  $\Omega^*$  and  $\dot{\Omega}^*$  to plan the feedforward torque input for the attitude dynamics. Feed-forward in the attitude regulation loop is a critical component of high-performance control and without this input, there will not be sufficient gain in the attitude dynamics to track aggressive attitude trajectories. However, computing the angular velocity goal that corresponds to a feedback dependent attitude control goal  $R^*$  in real-time requires forward prediction of the control trajectory using tools such as model predictive control (MPC) [52.8–10, 36]1. A simpler approach for trajectory tracking is to use the planned angular velocity  $\Omega^* = \Omega^p$  even though it does not exactly match the variation of  $R^*$ . As long as  $(\xi, \dot{\xi})$  is close to  $(\xi^*, \dot{\xi}^*) = (\xi^p, \dot{\xi}^p)$  then  $R^*$  is close to  $R^p$  and  $(\Omega^*, \dot{\Omega}^*) = (\Omega^p, \dot{\Omega}^p)$  will provide a good estimate of the critical feedforward attitude input.

We will discuss here the linear trajectory tracking algorithm for which the specified trajectory is required to have roll and pitch values that are small thus justifying a linear approximation of the dynamics. Accordingly, we assume that the Euler angles associated with the rotation  $R^p$  (52.1), are given by  $\theta^p = \phi^p = 0$ , while  $\psi^p$  is a specified function of  $t$ . For a given arbitrary yaw angle, we can linearize the dynamics about the hover position ( $\theta = 0, \phi = 0, \psi = \psi^p$ ) and the nominal inputs  $u_1 = mg, \mathbf{u}_2 = 0$ . Linearizing (52.2a), we obtain

$$\begin{aligned}\ddot{\xi}_1 &= g(\Delta\theta \cos \psi^p + \Delta\phi \sin \psi^p), \\ \ddot{\xi}_2 &= g(\Delta\theta \sin \psi^p - \Delta\phi \cos \psi^p), \\ \ddot{\xi}_3 &= \frac{1}{m}u_1 - g,\end{aligned}\quad (52.36)$$

where  $\Delta\theta = \theta^*$  and  $\Delta\phi = \phi^*$  represent the small deviations from the hover position. In order to exponentially drive all three components of error in the position part of the trajectory, we want the acceleration vector  $\ddot{\xi}$  to satisfy

$$(\ddot{\xi}^* - \ddot{\xi}) + K_d(\dot{\xi}^* - \dot{\xi}) + K_p(\xi^* - \xi) = 0.$$

From (52.36), we can immediately write

$$u_1 = m \left[ g + \ddot{\xi}_3^* + k_{d,z}(\dot{\xi}_3^* - \dot{\xi}_3) + k_{p,z}(\xi_3^* - \xi_3) \right], \quad (52.37)$$

to guarantee  $(\xi_3(t) - \xi_3^*(t)) \rightarrow 0$ . We choose the appropriate desired roll, pitch, and yaw angles for  $\theta^*, \phi^*,$

and  $\psi^*$  to guarantee exponential convergence:

$$\phi^* = \frac{1}{g}(\ddot{\xi}_1^* \sin \psi - \ddot{\xi}_2^* \cos \psi), \quad (52.38a)$$

$$\theta^* = \frac{1}{g}(\ddot{\xi}_1^* \cos \psi + \ddot{\xi}_2^* \sin \psi), \quad (52.38b)$$

$$\psi^* = \psi^p. \quad (52.38c)$$

Now  $(\psi^*, \phi^*, \theta^*)$  define the rotation matrix  $R^*$  (52.1) provided as a set point for the exponentially convergent attitude controller discussed in the previous section. Thus, as shown in Fig. 52.6, the control problem is addressed by decoupling the position control and attitude control subproblems and the position control loop provides the attitude set points for the attitude controller.

The position controller can also be obtained without linearization. This is done by projecting the position error (and its derivatives) along  $\mathbf{b}_3$  and applying the input  $u_1$  that cancels the gravitational force and provides the appropriate proportional plus derivative feedback

$$u_1 = m\mathbf{b}_3^T \left[ \ddot{\xi}^* + K_d(\dot{\xi}^* - \dot{\xi}) + K_p(\xi^* - \xi) + g\mathbf{e}_3 \right]. \quad (52.39)$$

Note that the projection operation is a nonlinear function of the roll and pitch angles and thus this is a nonlinear controller. In [52.7, 35], it is shown that this approach results in exponential stability and allows the robot to track trajectories in SE(3).

### 52.3.2 Control of Fixed-Wing Aircraft

An aircraft is a highly coupled nonlinear dynamical system and it may seem most natural to treat the control problem as an integrated multi-input multi-output (MIMO) nonlinear design [52.29, 38–40]. However, despite the nonlinear coupling of aircraft states there are still clear dependencies between specific actuators and certain dynamic modes of the open-loop response. A disadvantage of the MIMO approach is that it tends to obscure insight between control design and specific open-loop mode response. Moreover, and as a consequence, it tends to be less robust to large changes in model parameters (such as caused by using a different set of wings, or bolting on a completely new sensor package, not an uncommon situation for a small UAV system) than a classical control design. The classical, and more intuitive, control architecture for fixed wing vehicles is to consider a set of separate, but interconnected, single-input single-output (SISO) control loops. Such an approach has the advantage of being highly intuitive and leading to a modular design methodology



based on successive loop closure, providing a straight-forward gain tuning regime [52.31]. The robustness and simplicity of the SISO architecture make it the preferred choice for most small UAV control systems. A modern implementation, however, uses the total energy control system (TECS) architecture and input decoupling to overcome some of the limitations of classical fixed-wing control design.

The main control actions for a fixed wing aircraft are associated with the throttle, and the three aerodynamic control surfaces; rudder, ailerons, and elevators. The throttle regulates power to the motor and governs thrust  $T$ . The rudder, ailerons and elevators actuate the angular velocities  $\Omega_z$ ,  $\Omega_x$ , and  $\Omega_y$ , respectively, through the angular dynamics of the vehicle. For a small fixed-wing UAV in normal flight, a simple high-gain proportional control scheme will effectively regulate and decouple the variables  $(T, \Omega_x, \Omega_y, \Omega_z)$  [52.31]. The control problem can then be posed as one where  $(T, \Omega_x, \Omega_y, \Omega_z)$  are inputs for regulation of the remainder of the vehicle dynamics. Since there is weak physical coupling between the lateral variables (roll rate, bank angle, yaw rate, and course angle) and the longitudinal variables (airspeed, pitch rate, pitch angle, altitude rate, and altitude), and since the elevator and rudder most strongly effect the lateral variables and the throttle and aileron most strongly influence the longitudinal variables, most control architectures separate functionality into a lateral control system and a longitudinal control system. The input to the lateral control system is the desired course angle, and the input to the longitudinal control system is the desired airspeed and the desired altitude.

### Lateral Control System

There are three open-loop dynamic modes associated with the response of the lateral dynamics of a fixed-wing aircraft: the roll mode, the spiral mode, and the dutch roll mode. The *roll mode* is associated with the first-order response of the roll rate of the vehicle to aileron input. Usually the wings and airframe are designed (e.g., with a positive dihedral angle Chap. 26.4.4) so that this mode is highly stable and is regulated using high-gain in the aileron input – indeed, this mode is subsumed into the control simplification (regulation of  $\Omega_z$ ) proposed above.

The spiral mode is associated with the natural turning motion of the vehicle. That is, if the vehicle is banked into a turn, it will continue to turn until control action is applied to flatten the vehicle out. The spiral mode is a linearization of the bank-to-turn dynamics and is a single real pole close to the origin (Chap. 26, Fig. 26.22). Typically the spiral mode is slightly unstable due to the tendency of the vehicle to side-slip

into a turn. In manned flight, the spiral mode can be dangerous since there is very little external perception of turning. The nature of the banked turn dynamics ensure that the body-fixed-frame acceleration remains oriented through the central axis of the vehicle and rate of rotation is slow and nearly constant. The mode becomes dangerous if the pilot is not aware as the vehicle slowly side-slips down into the turn, progressively diving more and more steeply and increasing airspeed in what is known as a *spiral-dive*. For autonomous flight control, the spiral mode is relatively benign since autopilots never stop looking at the instruments and take immediate action if the vehicle is drifting off course.

The *dutch-roll* mode, is associated with the oscillation of the vehicle around a heading. In this motion, the vehicle yaws away from the heading and then rolls due to the dihedral effect, before the tilted lift vector and rudder action force the airplane back toward the incident wind. If the rudder is small and does not provide sufficient damping, the vehicle can overshoot to yaw and roll in the other orientation before repeating the oscillatory sequence. Dutch roll motion is less dangerous for manned flight since it is usually stable (except for vehicles with strongly swept back wings or negative dihedral) and produces unpleasant sideways acceleration with the side-slip motion that is immediately apparent to a pilot. Damping is increased by large tail plane surfaces and moderate to small dihedral. A figure of the typical pole positions of an aerobatic RC airplane is shown in Chap. 26, Fig. 26.22.

To understand the control problem for lateral dynamics, consider first the angular yaw velocity  $\Omega_z$  induced by rudder actuation. The primary effect of  $\Omega_z$  will yaw the vehicle in the air and generate nonzero side-slip  $\beta$ . In the *bank-to-turn* control paradigm described later, we will use  $\Omega_z$  to regulate  $\beta \equiv 0$ , however, it is instructive first to consider the effect of nonzero side-slip in order to build an intuitive understanding of the lateral dynamics. If the side-slip  $\beta \neq 0$ , the airplane will be sliding sideways or crabbing through the air. In particular, applying rudder input (nonzero  $\Omega_z$ ) acts to twist the airplane in the air; it does not in itself cause the trajectory of the airplane to curve. For a typical airplane with dihedral, this will lead the aircraft to bank away from the side-slip, and if the dutch-roll mode is stable, the airplane will settle into a banked turn. The causality of the system signals is given by

$$\Omega_z \rightarrow \beta \rightarrow \phi \rightarrow \chi.$$

Here the actuation from  $\beta \rightarrow \phi$  relies on the inherent stability of the dutch roll mode of the lateral open-loop dynamics of the airframe. Indeed, small-scale vehicles with strong dihedral and large tail planes can be flown

without aileron surfaces. For example, the aerial robotic vehicle as shown in Fig. 52.7, designed for slow low-level flight and equipped for visual terrain tracking using optic flow computed from a pair of downward pointing web cameras [52.41], does not have ailerons and the lateral motion is controlled using only the rudder.

This control paradigm has several negatives. It is rarely used for manned flight because side-slip motion generates sideways accelerations that do not feel natural. More importantly, the control response is limited by the low pass response of the open loop dutch roll dynamics of the aircraft. Although this mode is stable, there is often a noticeable damped oscillatory response that causes the vehicle trajectory to wander around the desired heading and degrades course tracking performance.

The alternative is to explicitly use the ailerons to impose the desired roll angle  $\phi$  on the vehicle and actuate the heading dynamics (52.27a) without using the rudder. The rudder then becomes a separate control input that can be used to regulate  $\beta$ . That is

$$\begin{aligned}\Omega_z &\rightarrow \beta, \\ \Omega_x &\rightarrow \phi \rightarrow \chi.\end{aligned}$$

Although, this may seem counter intuitive, (the rudder is not used to steer the airplane) it is, however, the most effective heading control strategy. Using this control strategy and regulating the side-slip  $\beta \equiv 0$  ensures that the bank-to-turn simplifications can be applied to the model as was shown in Sect. 52.2.3.

Specifically, in the bank-to-turn strategy where side-slip  $\beta$  is regulated to zero using the rudder, the lateral equations of motion are given by (52.24) and (52.27a). In level flight where the pitch angle is small and the velocity and angle of attack are roughly a constant, these



**Fig. 52.7** An autonomous fixed-wing aerial robot for experimental work on vision-based terrain tracking at ANU (after [52.41]). Note the upswept wings to generate dihedral and the lack of ailerons

equations simplify to the cascade structure

$$\begin{aligned}\dot{\phi} &= \Omega_x + d_\phi, \\ \dot{\chi} &= -A_\chi \phi + d_\chi,\end{aligned}$$

where  $A_\chi$  is a constant and  $d_\phi$  and  $d_\chi$  are disturbance signals introduced through the modeling process. From classical control theory, we know that a step in the heading command  $\chi^*$  can be tracked while simultaneously rejecting low-frequency disturbances  $d_\phi$  and  $d_\chi$  using a nested PI control law given by

$$\phi^* = k_{p_\chi}(\chi^* - \chi) + k_{I_\chi} \int_{-\infty}^t (\chi^* - \chi) d\tau, \quad (52.40)$$

$$\Omega_x = k_{p_\phi}(\phi^* - \phi) + k_{I_\phi} \int_{-\infty}^t (\phi^* - \phi) d\tau, \quad (52.41)$$

where  $k_{p_\chi}$ ,  $k_{I_\chi}$ ,  $k_{p_\phi}$ , and  $k_{I_\phi}$  are positive control gains. The proportional control

$$\Omega_z = -k_{p_\beta} \beta, \quad (52.42)$$

is usually effective at regulating the side-slip angle to zero, where  $k_{p_\beta}$  is a positive control gain.

### Longitudinal Control System

The longitudinal dynamics concern the thrust  $T$  and elevator (regulating  $\Omega_y$ ) inputs, along with the angle of attack  $\alpha$ , the flight path angle  $\gamma$ , the airspeed  $|v_a|$ , and the altitude  $h$ . There are two primary open-loop dynamic modes associated with the open loop response of the longitudinal dynamics, the short-period and phugoid modes. The *short-period* mode is associated with variation of pitch of the vehicle for constant velocity, constant altitude flight. It is a consequence of the linear dependence of lift of the primary wing to angle-of-attack as the vehicle pitches up and down around its center of the mass. The center of mass of an airplane is always designed to lie in front of the center of force of the primary wing surface to ensure that the short-period mode oscillation is stable, (placing the mass further forward increases the stability margin,) while damping provided by the tail plane of the vehicle ensures asymptotic stability (Chap. 26.4.2).

The *phugoid mode* is associated with the interplay of aerodynamic lift, velocity, glide path, and height of the vehicle for constant angle-of-attack flight. As a vehicle starts to descend gently, the airspeed increases as the loss of potential energy in height is transferred into kinetic energy. As the vehicle accelerates, the increased airspeed leads to increased primary lift on the wings leading the vehicle to pull out of the dive and to start to ascend again. The vehicle will slow as the

stored kinetic energy is traded back into potential energy. The resulting open-loop unstabilized motion is a repeated swooping cycle. Since aircraft are designed with low drag coefficients, the phugoid mode is usually very lightly damped, however, it is slow and easily stabilized. A key point to note in phugoid motion is that it is a constant energy oscillation; potential energy is transformed into kinetic energy and is then transformed back into potential energy.

Both thrust and pitch rate inputs affect both velocity and angle-of-attack of an airplane. In turn, the glide-path angle can be controlled through regulation of either angle-of-attack or velocity of the vehicle. The coupling associated with these dependencies mean that simple thrust to velocity or pitch-rate to glide-path SISO control loops cannot cover the full flight regime of a typical aircraft, a limitation of many existing autopilot systems even in commercial airliners. The industry standard approach to address this issue is to have different control modes for different flight conditions, take-off and climb, level flight, and descent, that exploit different input to state control mappings [52.31]. The total energy control system (TECS) design paradigm [52.42, 43] partially avoids these difficulties for a wide range of operating conditions and has the additional advantage of minimizing the control activity undertaken by the throttle.

Due to the energy preserving nature of the phugoid mode, small variations in velocity and height tend to be stable and energy conserving. Based on this insight, it is desirable to allow small variations of the airspeed of the vehicle as long as it is associated with the phugoid mode response. The key characteristic of the phugoid mode is that it preserve *total energy*

$$E := \frac{1}{2}m|v_a|^2 + mgh \quad (52.43)$$

of the aircraft. The TECS control architecture uses the total energy as an output and uses the throttle to regulate this output to a desired energy set point. The set point

$$E^*(t) := \frac{1}{2}m|v_a^*|^2 + mgh^*$$

is chosen to correspond to the desired trajectory. The energy error is

$$\tilde{E} := E^*(t) - E(t),$$

and the throttle input is assigned as

$$\delta_t = k_{p_E}\tilde{E}(t) + k_{i_E}\int_{-\infty}^t \tilde{E}(\tau) d\tau, \quad (52.44)$$

where  $k_{p_E}$  and  $k_{i_E}$  are positive control gains.

Once the throttle input is assigned, the remaining longitudinal dynamics must be controlled using the elevator to servo the pitch rate  $\Omega_y$ . The primary effect

of pitch rate is to rotate the wing section of the aircraft, directly effecting the angle-of-attack. Changing the angle-of-attack effects lift and drag generated by the wing, with lift most strongly effected since it depends linearly on  $\alpha$  (52.14) while drag is small and only varies with the square of the angle-of-attack (52.15). By definition, the lift  $L$  is the component of airfoil force that lies perpendicular to the velocity. As a consequence the lift force  $L$  does not contribute directly to changes in the total energy  $E$  of the vehicle. In particular, actuation of the pitch dynamics of the vehicle is (almost) decoupled from total energy regulation loop. It is now possible to choose an output for the elevator input and have confidence that the resulting SISO loop response will only marginally disturb the total energy regulation loop. Rather than simply regulate the height or velocity, both variables that have been considered as outputs for elevator regulation loops in classical fixed-wing control architectures [52.31], it is of interest to regulate a balance between kinetic and potential energy [52.42].

Consider the kinetic energy and potential energy of the vehicle separately

$$K = \frac{1}{2}m|v_a|^2, \quad U := mgh.$$

A given flight trajectory corresponding to desired values of  $(|v_a^*(t)|, h^*(t))$  defines desired set points for kinetic and potential energy  $K^*(t) = \frac{1}{2}m|v_a^*(t)|^2$  and  $U^* = mgh^*(t)$ . Define the errors in the kinetic and potential energy along the trajectory as

$$\begin{aligned} \tilde{K} &= K^*(t) - K(t) = \frac{1}{2}m[|v_a^*(t)|^2 - |v_a(t)|^2], \\ \tilde{U} &= U^*(t) - U(t) = mg[h^*(t) - h(t)], \end{aligned} \quad (52.45)$$

and define the combined energy balance error  $\tilde{B}$  by

$$\tilde{B} = \tilde{K} - \tilde{U}.$$

The proposed control strategy is to use the commanded pitch angle  $\theta^*$  to regulate  $\tilde{B} \rightarrow 0$ .

To understand this control architecture, note that if  $\tilde{E} = 0$  then  $\tilde{K} = \tilde{E} - \tilde{U} = -\tilde{U}$  and hence

$$\tilde{B} = 2\tilde{K} = -2\tilde{U}.$$

It follows that driving  $\tilde{B}$  to zero forces both  $|v_a| \rightarrow |v_a^*|$  and  $h \rightarrow h^*$ . The real advantage of the balanced energy control architecture occurs when  $\tilde{E} \neq 0$ . In this case, driving  $\tilde{B} \rightarrow 0$  will not force either  $|v_a|$  or  $h$  to its reference set point at all costs, but rather, it will balance the excess or deficit energy between kinetic and potential energy set points around the desired trajectory.

Balancing the energy error in this way is a highly robust control strategy that maximizes the ability of the throttle to maintain good control of the total energy.

An additional insight is that the difference of the energy terms  $\tilde{B}$  is maximally sensitive to excitation in the phugoid mode. In particular, if power flows between potential and kinetic energy levels, then the relative variation in  $\tilde{B}$  is maximal compared to any other combined measure incorporating  $|v_a|$  and  $h$  subject to scaling factors. Thus, the balanced energy control strongly directly damps the phugoid mode that is uncontrolled by the thrust control.

The desired pitch angle is therefore given by

$$\theta^* = k_{p_B} \tilde{B}(t) + k_{I_B} \int_{-\infty}^t \tilde{B}(\tau) d\tau, \quad (52.46)$$

where  $k_{p_B}$  and  $k_{I_B}$  are positive control gains. In practice, the pitch angle actuates stable angle-of-attack dynamics that in turn lead to regulation of the flight-path angle and finally control the tradeoff encoded in  $\tilde{B}$ . The stability of the internal dynamics for the proposed SISO control loop are handled by suitable tuning of the PI gains, avoiding the need to explicitly model these dynamics. The effectiveness and robustness of this approach is well established in the literature [52.31].

### Control Implementation and Gain Tuning

The lateral control strategy for fixed wing aircraft is based on (52.40), (52.41), and (52.42). In using these commands, we are assuming high-bandwidth feedback loops regulating  $\Omega_x$  and  $\Omega_z$  using the ailerons and rudder, respectively. Practical implementation of the lateral control loops required saturating the roll command  $\phi^*$  to  $\pm\bar{\phi}$ , where, for most airframes, a reasonable value is  $\bar{\phi} = 30^\circ$ . Commanding higher roll angles usually results in large side-slip angles, which leads to unacceptably large drops in altitude during turns. The roll rate command  $\Omega_x$  is also saturated to a fraction of the limits of the rate gyro sensor to ensure adequate convergence of the attitude estimator. Practical implementation of (52.40) also requires careful wrapping of the angles  $\chi$  and  $\chi^*$  around  $\pm 180^\circ$  to avoid large heading errors that result in not associating  $180^\circ$  with  $-180^\circ$ .

The gains of the lateral control loops can be tuned in flight by selectively enabling one loop at a time. A strategy that has proven success over numerous flight test is to tune the gains in the following order:

1. Attitude rate loops regulating  $\Omega_x$  and  $\Omega_z$ .
2. Side slip gain  $k_{p_\beta}$ .
3. The proportional gain on roll error  $k_{p_\phi}$ , followed by the integral gain  $k_{I_\phi}$ . The integral gain  $k_{I_\phi}$  is often

set to zero, since the integrator on the heading loop provides suitable robustness.

4. The proportional gain on the heading loop  $k_{p_\chi}$ , followed by the integral gain  $k_{I_\chi}$ .

The use of (52.46) assumes a high-bandwidth pitch control loop using the elevator as an actuator. Practical implementation of (52.44) requires saturating  $\delta_i$  above by  $\delta_i^{\max}$  and below by  $\delta_i^{\min} \geq 0$ . Saturating the pitch angle is also critical to avoid stall conditions that occur at large angles of attack. An effective method to do this is to saturate the altitude error in computing the error in potential energy, replacing (52.45) with

$$\tilde{U} = mg \text{sat}[h^*(t) - h(t), \bar{h}], \quad (52.47)$$

where

$$\text{sat}(x, \ell) = \begin{cases} \ell & \text{if } x \geq \ell, \\ -\ell & \text{if } x \leq -\ell, \\ x & \text{otherwise.} \end{cases}$$

Saturating the altitude error will cause a steady climb rate when  $h^* - h$  is large. To understand why, assume that velocity is well regulated, and that the altitude error is large, then  $\tilde{B} \approx -mg \text{sat}(h^* - h, \bar{h}) = -mg\bar{h}$ . Ignoring the integrator, this will cause a constant pitch angle command from (52.46). However, simply saturating the pitch angle will not result in good performance since driving

$$\begin{aligned} \tilde{B} = \tilde{K} - \tilde{U} = & \frac{1}{2}m(|v_a^*(t)|^2 - |v_a(t)|^2) \\ & - mg[h^*(t) - h(t)] \end{aligned}$$

to zero will cause errors in kinetic and potential energy to balance. Therefore, a large unsaturated altitude error will result in the controller increasing the airspeed error. A sustained altitude error will cause the integrator in (52.46) to wind up. Therefore, an integrator antiwindup scheme is essential.

Similar to the lateral control loop, the gains for the longitudinal controller can be tuned in flight by selectively enabling one loop at a time. The gains should be tuned in the following order:

1. The pitch attitude loops is first tuned. Pitch attitude is typically controlled using a PID controller. The derivative gain can be tuned to provide adequate damping on the RC controller. The proportional gain is then added and adjusted to provide adequate transient response. The integrator is added afterward to remove steady state error in pitch.
2. The throttle gains  $k_{p_E}$  and  $k_{I_E}$  in (52.44) are then adjusted. We have found that normalizing the energy error  $\tilde{E}$  by the reference kinetic energy  $K^{\text{ref}} = \frac{1}{2}m|v_a^{\text{ref}}|$  makes these gains particularly easy to tune,

and that the scaling results in similar gains working across different platforms.

3. The energy balance gains  $k_{p_B}$  and  $k_{I_B}$  are tuned last. Again, scaling  $\tilde{B}$  by  $K^{\text{ref}}$  seems to simplify the tuning process for different airframes.

An advantage of the TECS is that it reduces the need for different control modes for the longitudinal autopilot. In particular, the *altitude hold mode*, the *climb mode*, and the *descend mode* described in [52.31] are reduced to one mode using TECS. However, we should

note that the *take-off mode* described in [52.31] is still needed for this scheme. For small aircraft that are hand launched, or any aircraft whose velocity at take off is significantly below the commanded velocity, the TECS control in (52.46) will cause the vehicle to pitch down to gain airspeed when the airspeed error is large. This pitch-down behavior will cause the airframe to crash if it is executed immediately after take-off. Therefore, the best strategy is to apply full throttle immediately after take-off, and to set the commanded pitch angle to fixed value that is adequate for a climb rate that avoids stall.

## 52.4 Trajectory Planning

There are many different control tasks that aerial robotic vehicles will be required to undertake in the coming years. In this chapter, it is impossible to cover the whole range of potential tasks along with their associated planning problems. We will consider only basic trajectory or path planning problems for both quadrotor and fixed-wing vehicles. This problem is fundamental to fixed-wing navigation where the distances involved are such that path and trajectory planning is sufficient for almost all goals. For small aerial robotic vehicles flying in cluttered 3-D-spaces, there is a much wider selection of goals including things such as, physical interaction with the environment, obstacle avoidance, etc., as well as simply planning and following a trajectory to a given way-point. However, the trajectory planning provides a basic building block in achieving a wide range of goals, and is a necessary component of achieving high-performance tasks.

### 52.4.1 Trajectory Planning for Quadrotors

The quadrotor is underactuated and this makes it difficult to plan trajectories in 12-dimensional state space (6DOF position and velocity). However, the problem is considerably simplified if we use the fact that the quadrotor dynamics are differentially flat [52.44]. To see this, we consider the output position  $\xi$  and the yaw angle  $\psi$ . We show that we can write all state variables and inputs as functions of the outputs  $(\xi, \psi)$  and their derivatives. Derivatives of  $\xi$  yield the velocity  $v$ , and the acceleration,

$$\dot{v} = \frac{1}{m} u_1 \mathbf{b}_3 + g \mathbf{e}_3.$$

From Fig. 52.3, we see that

$$\mathbf{d}_1 = [\cos \psi, \sin \psi, 0]^T$$

and the unit vectors for the body-fixed frame, can be written in terms of the variables  $\psi$  and  $\dot{\psi}$  as follows

$$\mathbf{b}_3 = \frac{\dot{\psi} - g \mathbf{e}_3}{\|\dot{\psi} - g \mathbf{e}_3\|}, \mathbf{b}_2 = \frac{\mathbf{b}_3 \times \mathbf{d}_1}{\|\mathbf{b}_3 \times \mathbf{d}_1\|}, \mathbf{b}_1 = \mathbf{b}_2 \times \mathbf{b}_3$$

provided  $\mathbf{b}_3 \times \mathbf{d}_1 \neq 0$ . This defines the rotation matrix  ${}^A R_B$  as a function of  $\dot{\psi}$  (the second derivative of  $\xi$ ) and  $\psi$ . In this way, we write the angular velocity and the four inputs as functions of the position, velocity ( $v = \dot{\xi}$ ), acceleration ( $a = \ddot{\xi}$ ), jerk ( $\gamma = \xi^{(iii)}$ ), and snap or the derivative of jerk ( $\sigma = \xi^{(iv)}$ ). From these equations, it is possible to verify that there is a diffeomorphism between the  $18 \times 1$  vector

$$\mathbf{X} = (\xi^T, v^T, a^T, \gamma^T, \sigma^T, \psi^T, \dot{\psi}^T, \ddot{\psi}^T)^T$$

and the state augmented with the inputs and their derivatives

$$(\xi^T, \dot{\xi}^T, R, \Omega^T, u_1, \dot{u}_1, \ddot{u}_1, \mathbf{u}_2^T)^T.$$

This property of differential flatness makes it easy to design trajectories that respect the dynamics of the underactuated system. Any four-times-differentiable trajectory in the space of flat outputs,  $(\xi^T(t), \psi(t))^T$ , corresponds to a feasible trajectory, one that satisfies the equations of motion. All inequality constraints of states and inputs can be expressed as functions of the flat outputs and their derivatives. This mapping to the space of flat outputs can be used to generate trajectories that minimize a cost functional formed by a weighted combination of the different flat outputs and





then the Dubins car path must be suitably modified. One alternative is to fly at the flight path angle constraint while making multiple complete orbits on the minimum turn radius helix at the beginning of the Dubins car path before proceeding along the straight line segment of the path. Of course, a similar strategy would be to make multiple complete orbits on the minimum turn radius helix at the end of the Dubins car path. Such paths are termed *high-altitude paths* in [52.51]. The middle case is when the flight path angle constraint does not allow sufficient altitude gain/loss following the Dubins car path, but where one complete orbit along the start or end circle of the Dubins car path at the maximum flight path angle results in more altitude gain/loss than is needed. In this case, a deviation can be placed in the Dubins car path to extend the path length to just the right amount so that the altitude gain/loss can be achieved while flying at the flight path angle constraint. These paths are termed *medium-altitude paths* in [52.51].

Following the notation defined in [52.52] let  $L_{\text{car}}(C_s, C_e, R)$  denote the path length of the Dubins car path between the projection of the start configuration  $C_s$  onto the North–West plane, and the projection of the end configuration  $C_e$  onto the North–West plane, using  $R$  as the turn radius of the vehicle.

#### Low-Altitude Dubins Paths

The altitude gain between the start and end configuration is said to be *low altitude* if

$$|h_e - h_s| \leq L_{\text{car}}(C_s, C_e, R_{\min}) \tan \bar{\gamma},$$

where the term on the right is the maximum altitude gain that can be obtained by flying at flight-path angle  $\pm \bar{\gamma}$  for a distance of  $L_{\text{car}}(C_s, C_e, R_{\min})$ .

In the low-altitude case, the altitude gain between the start and end configurations can be achieved by flying the Dubins car path with a flight-path angle satisfying  $|u_2| \leq \bar{\gamma}$ . Therefore, the optimal flight-path angle can be computed by

$$u_2^* = \tan^{-1} \left( \frac{|h_e - h_s|}{L_{\text{car}}(C_s, C_e, R_{\min})} \right).$$

#### Medium-Altitude Dubins Paths

The altitude gain between the start and the end configuration is said to be *medium altitude* if

$$\begin{aligned} L_{\text{car}}(C_s, C_e, R_{\min}) \tan \bar{\gamma} &< |h_e - h_s| \\ &\leq [L_{\text{car}}(C_s, C_e, R_{\min}) + 2\pi R_{\min}] \tan \bar{\gamma}, \end{aligned} \quad (52.49)$$

where the addition of the term  $2\pi R_{\min}$  accounts for adding one orbit at radius  $R_{\min}$  to the path length.

In the medium-altitude case, the altitude difference between the start and end configurations is too large to

obtain by flying the Dubins car path at the flight-path angle constraint, but small enough that adding a full turn on the helix at the beginning or end of the path and flying so that  $\gamma = \pm \bar{\gamma}$  results in more altitude gain/loss than is needed. As shown in [52.51], the minimum distance path is achieved by setting  $\gamma = \text{sign}(h_e - h_s) \bar{\gamma}$  and inserting an extra maneuver in the Dubins car path that extends the path length so that the altitude gain when  $\gamma = \pm \bar{\gamma}$  is exactly  $|h_e - h_s|$ . While there are numerous possible ways to extend the path length, the method proposed in [52.52] is to add an additional intermediate arc to the start or end of the path, as shown in Figs. 52.8 and 52.9. If the start altitude is lower than the end altitude, then the intermediate arc is inserted immediately after the start helix. If on the other hand, the start altitude is higher than the end altitude, then the intermediate arc is inserted immediately before the end helix.

#### High-Altitude Dubins Paths

The altitude gain between the start and end configurations is said to be *high altitude* if

$$|h_e - h_s| > [L_{\text{car}}(C_s, C_e, R_{\min}) + 2\pi R_{\min}] \tan \bar{\gamma}.$$

In the high-altitude case, the altitude gain cannot be achieved by flying the Dubins car path within the flight-path angle constraints. As shown in [52.51], the minimum distance path is achieved when the flight-path angle is set at its limit of  $\pm \bar{\gamma}$ , and the Dubins car path is extended to facilitate the altitude gain. While there are many different ways to extend the Dubins car path, [52.52] suggests extending the path by spiraling a certain number of turns at the beginning or end of the path, and then by increasing the turn radius by the appropriate amount.

For UAV scenarios, the most judicious strategy is typically to spend most of the trajectory at as high an altitude as possible. Therefore, if the altitude at the end configuration is higher than the altitude at the start configuration, then the path will be extended by a climbing helix at the beginning of the path. If on the other hand, the altitude at the start configuration is higher than the end configuration, then the path will be extended by a descending helix at the end of the path. If multiple turns around the helix are required, then the turns could be split between the start and end helices and still result in the same path length. For high-altitude Dubins paths, the required number of turns in the helix will be the smallest integer  $k$  such that

$$\begin{aligned} [L_{\text{car}}(C_s, C_e, R_{\min}) + 2\pi k R_{\min}] \tan \bar{\gamma} &\leq |h_e - h_s| \\ &< [L_{\text{car}}(C_s, C_e, R_{\min}) + 2\pi(k+1)R_{\min}] \tan \bar{\gamma}, \end{aligned} \quad (52.50)$$

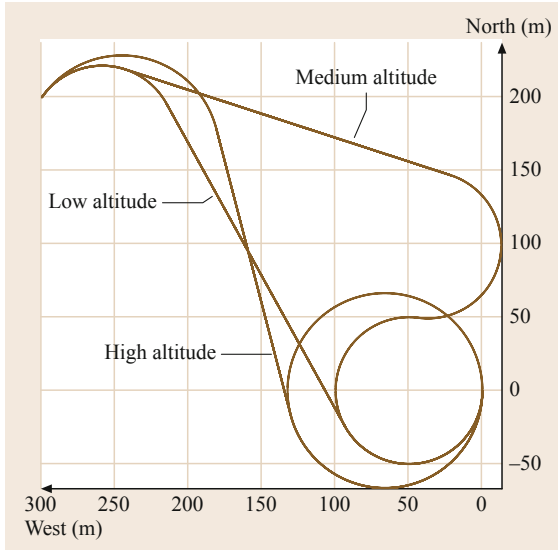


**Fig. 52.8** A top down view of low altitude, medium altitude, and high-altitude Durbin airplane paths. The initial and end configurations are identical except for the final altitude

or in other words

$$k = \left\lfloor \frac{1}{2\pi R_{\min}} \left[ \frac{|h_e - h_s|}{\tan \bar{\gamma}} - L_{\text{car}}(C_s, C_e, R_{\min}) \right] \right\rfloor,$$

where  $\lfloor x \rfloor$  is the floor function that rounds  $x$  down to the nearest integer. The radius of the start and end helices is then increased to  $R^*$  so that

$$\left[ L_{\text{car}}(C_s, C_e, R^*) + 2\pi k R^* \right] \tan \bar{\gamma} = |h_e - h_s|. \quad (52.51)$$

Figures 52.8 and 52.9 show two perspective of three different Dubins airplane paths that start and end in the same configuration with the exception of the final altitude, which changes from 250 m for the low-altitude path, to 350 m for the medium-altitude path, to 450 m for the high-altitude path. A top down view is shown in Fig. 52.8. Note that for both the low-altitude and medium-altitude paths, that the minimum turn radius constraint is active, whereas for the high-altitude path, the turn radius in the turns is larger than the minimum turn radius constraint. A three-dimensional view

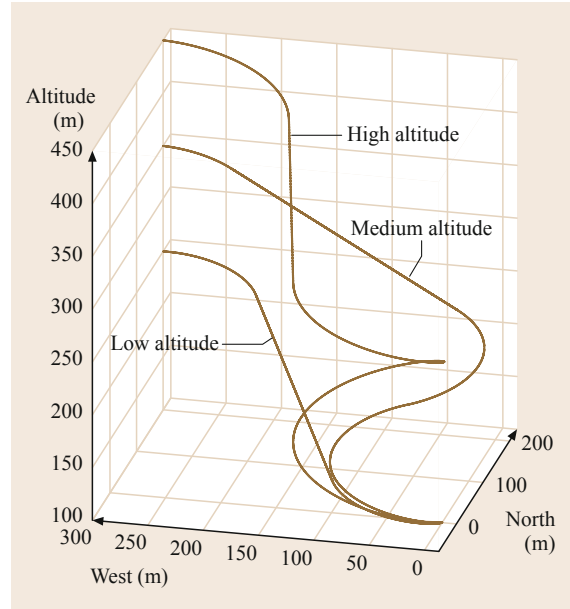


**Fig. 52.9** A three-dimensional view of low altitude, medium altitude, and high-altitude Durbin airplane paths. The initial and end configurations are identical except for the final altitude

is shown in Fig. 52.9. Note that for both the medium- and high-altitude paths, the flight path angle constraint is active, but that it is not active for low-altitude paths.

There are a variety of techniques that allow the control architecture described in Sect. 52.3.2 to follow Dubins airplane paths. A simple method is to parameterize the path using a path parameter  $\sigma$ . Suppose that the resulting parameterized path is given by  $p(\sigma)$ . At each sample time, the path parameter is advanced along the path so as to minimize the distance to the path from the aircraft

$$\sigma_{t+1} = \arg \min_{s \geq \sigma_t} \|\xi(t) - p(s)\|,$$

where  $\xi(t)$  is the inertial position of the aircraft. The commanded airspeed  $|v_a^*|$ , course angle  $\chi^*$ , and altitude  $h^*$  at time  $t$  are then given by the parameterized Dubins airplane path  $p(\sigma_{t+1})$ . This technique is similar to the guidance strategy suggested in [52.53]. Alternative method based on vector field methods are described in [52.54–56].

## 52.5 Estimating the Vehicle State

A critical aspect in implementation of real world aerial robotic vehicles is providing good estimates of the state of the vehicle. The key state estimates required for control of an aerial vehicle are associated with the rigid-body dynamics of its airframe, height, attitude, angular velocity, and linear velocity. Moreover, fixed-wing vehicle dynamics depend on the aerodynamics states of angle-of-attack and side-slip angle. Of these states, the attitude and angular velocity are the most important as they are the primary variable used in attitude control and flight-regulation of the vehicle. Angle-of-attack and side-slip angles are rarely estimated explicitly and are dealt with as internal dynamics in the control design rather than explicit outputs or disturbances.

The ubiquitous instrumentation carried by any aerial vehicle is an inertial measurement unit (IMU) often augmented by some form of height measurement, either acoustic, infra red, barometric, or laser based. Vehicles that fly in outside environments carry a GPS system, most of which now provide velocity estimation as well as position. Many fixed wing vehicles also include a pitot tube (for dynamic pressure) or an anemometer to measure forward velocity. Indoor aerial robotic vehicles in research laboratories are often flown in flight environments equipped with motion capture systems like VICON or Optitrack [52.5, 6]. Finally, many aerial robotic systems have also been equipped with exteroceptive sensor systems including Kinect 3D-range cameras, scanning laser rangefinder, integrated stereo camera systems, or simple monocular cameras. There is an active research field in developing 3-D-SLAM (simultaneous localization and mapping; Chap. 46.4) algorithms for mapping and localization of aerial robotic vehicles.

The rigid-body dynamic state is crucial to the control performance of an aerial robotic system and we will concentrate on this estimation problem in this chapter. A natural approach to state-estimation is to apply classical filter design to a coordinate representation of the rigid-body state. A good development of this approach for small-scale aerial robotic systems is presented in [52.31]. An alternative approach is to exploit the nonlinear structure of the rigid-body kinematics to develop nonlinear observers. This approach has been shown to generate simple, robust, and highly effective filters for small-scale aerial robotic systems, especially for the key problem of attitude estimation.

### 52.5.1 Estimating Attitude

A typical IMU includes a three-axis rate gyro, three-axis accelerometer, and three-axis magnetometer. The

rate gyro measures angular velocity of  $\{B\}$  relative to  $\{A\}$  expressed in the body-fixed-frame of reference  $\{B\}$

$$\Omega_{\text{IMU}} = \Omega + b_{\Omega} + \eta \in \{B\},$$

where  $\eta$  denotes additive measurement noise and  $b_{\Omega}$  denotes a constant (or slowly time-varying) gyro bias. Generally, the gyroscopes installed on quadrotor vehicles are lightweight MEMS devices that are reasonably robust to noise and quite reliable.

The accelerometers (in a *strap down IMU configuration*) measure the instantaneous linear acceleration of  $\{B\}$  due to exogenous force

$$a_{\text{IMU}} = R^T(\dot{v} + ge_3) + b_a + \eta_a \in \{B\}, \quad (52.52)$$

where  $b_a$  is a bias term,  $\eta_a$  denotes additive measurement noise, and  $\dot{v}$  is in the inertial frame. Accelerometers are highly susceptible to vibration and mounted on a typical aerial robotic platform they require significant low-pass mechanical and/or electrical filtering to be reliable. Most vehicles avionics will incorporate an analogue anti-aliasing filter on a MEMS accelerometer before the signal is sampled.

The magnetometers provide measurements of the ambient magnetic field

$$m_{\text{IMU}} = R^T {}^A m + B_m + \eta_b \in \{B\},$$

where  ${}^A m$  is the Earth's magnetic field vector (expressed in the inertial frame),  $B_m$  is a body-fixed-frame expression for the local magnetic disturbance and  $\eta_b$  denotes measurement noise. The noise  $\eta_b$  is usually quite low for magnetometer readings, however, the local magnetic disturbance  $B_m$  can be very significant, especially if the sensor is placed near power cables for the motors.

In outdoor environments, the GPS is typically used to provide position, inertial velocity, and course angle. The GPS system consists of a constellation of 24 satellites that continuously orbit the earth at an altitude of 20 180 km. The position of a GPS receiver is determined by observing the time-of-flight of signals sent from the satellites and detected by the receiver. If accurate timing information is available at the receiver, then a minimum of three satellites signals are necessary to resolve the position of the receiver. However, for low-cost GPS receivers, timing information must also be received and this requires a minimum of four satellite signals. A variety of factors effect the accuracy of GPS estimates. The dominant sources of error include inaccurate satellite orbital data, inaccuracy in the satellite clocks, variable signal delay as it passes through

the ionosphere, weather conditions near the earth surface, and multipath reflections from nearby buildings and mountains. Total GPS bias error is approximately 5–10 m. Modern GPS receivers exploit doppler shift in the carrier phase of the received signals to estimate the course angle  $\chi$  and the ground speed.

The accelerometers and magnetometers can be used to provide absolute attitude information on the vehicle while the rate gyroscope provides complementary angular velocity measurements. The attitude information in the magnetometer signal is straightforward to understand; in the absence of noise and bias then  $m_{\text{IMU}}$  provides a body-fixed frame measurement of  $R^T A m$ , and consequently constrains two degrees of freedom in the rotation  $R$ . The accelerometer can also be used as long as the component of acceleration associated with the inertial motion of the vehicle is compensated. The simplest way in which to do this is to use an absolute external signal such as GPS to estimate the vehicle acceleration

$$a_{\text{CTD}} = a_{\text{IMU}} - \hat{R}^T \ddot{\xi}_{\text{GPS}},$$

where  $a_{\text{CTD}}$  is the corrected acceleration. In this case,  $a_{\text{CTD}} \approx R^T e_3$  and this provides attitude information. It is important to note that in the complementary filter proposed below (52.53), only the low-frequency component of  $a_{\text{CTD}}$  is required. As such, the potential noise in the second derivative of a GPS signal  $\ddot{\xi}_{\text{GPS}}$  is not necessarily the problem that may be initially feared. The key to good filter performance is to ensure that the cross over frequency of the complimentary sensitivity is low enough that any phase distortion associated with low-pass filtering of  $\ddot{\xi}_{\text{GPS}}$  does not effect the estimate.

#### Remark 52.1

There may be issues in applying the correction  $\hat{R}^T \ddot{\xi}_{\text{GPS}}$  if there is a delay in receiving the GPS signals. This can be addressed, at the cost of storing IMU data, by combining a short time prediction along with a time-lagged observer [52.57].

In the case where GPS or an external measure of the vehicles motion is not available, there are a number of alternative techniques available to use the accelerometer information for attitude estimation. For fixed-wing vehicles, the most important disturbance is due to centripetal acceleration due to the vehicle turning. It is possible to model the centripetal acceleration using airspeed and angular velocity and compensate using a feedforward term [52.58, 59]. In the case of rotorcraft in mostly hover flight conditions, it turns out

that using the raw IMU accelerometer readings still works extremely well [52.60–62] due to the disturbance caused by the aerodynamic drag term  $\Delta = -Dv$  (52.10) [52.21, 24, 25, 63]. In this case the corrected accelerometer  $a_{\text{CTD}}$  used in the filter (52.53) below is just the raw IMU accelerometer measurement.

The attitude kinematics of the quadrotor are given by (52.2c). Let  $\hat{R}$  denote an estimate for attitude  $R$  of the quadrotor vehicle. The following observer [52.61, 62] fuses accelerometer, magnetometer, and gyroscope data as well as other direct attitude estimates  $R_E$  (such as provided by a VICON or other external measurement system) should they be available

$$\dot{\hat{R}} := \hat{R} \left( \Omega_{\text{IMU}} - \hat{b} \right)_{\times} - \gamma, \quad (52.53a)$$

$$\dot{\hat{b}} := k_b \gamma, \quad (52.53b)$$

$$\begin{aligned} \gamma := & \left( \frac{k_a}{g^2} \left[ (\hat{R}^T e_3) \times a_{\text{CTD}} \right] \right. \\ & + \frac{k_m}{A m^2} \left[ (\hat{R}^T A m) \times m_{\text{IMU}} \right] \Big)_{\times} \\ & + k_E \mathbb{P}_{\mathfrak{so}(3)} \left( \hat{R} \hat{R}_E^T \right), \end{aligned} \quad (52.53c)$$

where  $k_a$ ,  $k_m$ ,  $k_E$ , and  $k_b$  are arbitrary nonnegative observer gains and  $\mathbb{P}_{\mathfrak{so}(3)}(M) = (M - M^T)/2$  is the Euclidean matrix projection onto the skew-symmetric matrices. If any one of the measurements in the innovation  $\gamma$  are not available or unreliable, then the corresponding gain should be set to zero in the observer. Note that both the attitude  $\hat{R}$  and the bias corrected angular velocity  $\hat{\Omega} = \Omega_{\text{IMU}} - \hat{b}$  are estimated by this observer. The observer (52.53) has been extensively studied in the literature [52.61, 62] and shown to converge exponentially (both theoretically and experimentally) to the desired attitude estimate of attitude with  $\hat{b}$  converging to the gyroscope bias  $b$ . The filter has a complementary nature, using the high-frequency part of the gyroscope signal and the low-frequency parts of the magnetometer, accelerometer, and external attitude measurements [52.61]. The roll off frequencies associated with each of these signals is given by the gains  $k_a$ ,  $k_m$ , and  $k_E$  in rad/s.

### 52.5.2 Estimating Velocity and Position

Estimating velocity and position is a straightforward process if the vehicle is equipped with a GPS system. In this case, the dynamics (52.2a) and (52.2b) are linear, and a linear filter can be used. Let  $\hat{\xi}$  denote the estimate of position and  $\hat{v}$  denote the estimate of velocity. A sim-



ple linear filter is given by

$$\begin{aligned}\dot{\hat{\xi}} &= \hat{v} - k_x(\hat{\xi} - \xi_{\text{GPS}}), \\ \dot{\hat{v}} &= \hat{R}^T a_{\text{IMU}} - g e_3 - k_v(\hat{\xi} - \xi_{\text{GPS}}),\end{aligned}$$

for gains  $k_x, k_v > 0$ . As long as the attitude estimate  $\hat{R}$  is accurate, this filter design is highly robust. It is easily possible to add bias estimates for the accelerometer if desired. Equally well it is straightforward to use Kalman filter techniques to tune the gains  $k_x$  and  $k_v$  in real-time if that is considered advisable. In practice, for small aerial robotic systems, the noise characteristics of the measurements are so poor that it is often best to use a constant gain filter rather than introduce the additional complexity and potential instability of the Riccati equation associated with a Kalman filter.

In the absence of GPS, estimating position depends on the availability of additional sensor systems. Since most aerial robots are equipped with a barometer to provide an estimate of height and this can be utilized for an estimate of the vertical motion of the vehicle

$$\dot{\hat{h}} = \hat{v}_z - k_h(\hat{h} - h), \quad (52.54a)$$

$$\dot{\hat{v}}_z = e_3^T \hat{R}^T a_{\text{IMU}} - g - k_{v_z}(\hat{h} - h), \quad (52.54b)$$

where  $k_h, k_{v_z} > 0$  are positive gains.

For quadrotor vehicles, there is also the possibility of exploiting the linear drag aerodynamic forces (52.10) associated with blade flapping and induced drag to estimate horizontal velocity for a vehicle in near hover conditions [52.24]. Define a projector matrix

$$\mathbb{P}_h := \begin{pmatrix} 1 & 0 & 0 \\ 0 & 1 & 0 \end{pmatrix} \quad (52.55)$$

that takes the first two components of a vector. Then the horizontal component of the *inertial* acceleration can be measured by

$${}^A a_h := \mathbb{P}_h {}^A a = \mathbb{P}_h R a \approx \mathbb{P}_h \hat{R} a, \quad (52.56)$$

where we assume that the estimate  $\hat{R}$  is close to  $R$ . If we assume the vehicle is only slowly varying in height one has  $v_z \approx 0$  in comparison to horizontal velocity

$$v_h \approx \mathbb{P}_h^T v.$$

Furthermore, the thrust  $T \approx mg$  must compensate the weight of the vehicle. Recalling (52.10) and taking just the horizontal component one has

$${}^A a_h \approx -g \mathbb{P}_h \hat{R} e_3 - g \mathbb{P}_h \hat{R} \hat{R}^T \mathbb{P}_h^T v_h. \quad (52.57)$$

If the attitude filter estimate is good and the assumptions about vehicle motion hold then (52.56) and (52.57) can be solved for an estimate of  $v_h$

$$v_h \approx -\frac{1}{g} \left( \mathbb{P}_h \hat{R} \hat{R}^T \mathbb{P}_h^T \right)^{-1} \left( {}^A a_h + g \mathbb{P}_h \hat{R} e_3 \right). \quad (52.58)$$

Equation (52.58) provides a measurement of the horizontal velocity, however, since it directly incorporates the unfiltered accelerometer readings it is generally too noisy to be of much use. Its low-frequency content can, however, be used to drive a velocity complementary observer that uses the attitude estimate and the system model (52.2b). Let  $\hat{v}_h$  be an estimate of the horizontal component of the inertial velocity of the vehicle then an observer is given by

$$\dot{\hat{v}}_h = -g \mathbb{P}_h^T (\hat{R} e_3 + \hat{R} \hat{R}^T \mathbb{P}_h^T \hat{v}_h) - k_w(\hat{v}_h - v_h), \quad (52.59)$$

where  $v_h$  is given by (52.58). The gain  $k_w > 0$  provides a tuning parameters that indicates the roll-off frequency for the information from  $\hat{v}_h$  that is used in the filter. It also uses estimated velocity  $\hat{v}_h$  to provide an approximation of the more correct  $\hat{R} \hat{R}^T \mathbb{P}_h^T v_h$  term in the feedforward velocity estimate, however, since the underlying dynamics associated with this term is stable, then the observer is stable even with this approximation. It is found that this observer works remarkably well in practice for quadrotor vehicles that are not engaged in acrobatic maneuvers [52.21, 24, 25, 63].

## 52.6 Conclusion



This chapter has focused on the fundamental technology associated with making an aerial robotic system operate effectively and efficiently. In particular, we have focused on the design of control and navigation algorithms, and along with that the associated questions of modeling and state estimation. Once a robust and reliable aerial robotic platform is available, the range of

potential applications for unmanned aerial systems is vast. An indication of the potential is given by a list of application categories that are already under consideration [52.64, 65]: *Remote sensing* such as pipeline spotting, power-line monitoring, volcanic sampling, mapping, meteorology, geology, and agriculture [52.66, 67], as well as unexploded mine detection [52.68].

*Disaster response* such as chemical sensing, flood monitoring, and wildfire management. *Surveillance* such as law enforcement, traffic monitoring, coastal and maritime patrol, and border patrols [52.69]. *Search and rescue* in low-density or hard-to-reach areas. *Transportation* including small and large cargo transport, and possibly passenger transport. *Communications* as permanent or *ad hoc* communication relays for voice

and data transmission, as well as broadcast units for television or radio. *Payload delivery* for a wide range of applications including agriculture, firefighting, and even logistics of product delivery. *Image acquisition* for cinematography and real-time entertainment. It is no surprise that aerial robotics is one of the most dynamic and exciting fields of robotics research at the moment.

## Video-References

-  **VIDEO 436** Autopilot using total energy control  
available from <http://handbookofrobotics.org/view-chapter/52/videodetails/436>
-  **VIDEO 437** Dubins airplane  
available from <http://handbookofrobotics.org/view-chapter/52/videodetails/437>

## References

- 52.1 R.C. Michelson: International aerial robotics competition – The world's smallest intelligent flying machines, 13th RPVs/UAVs International Conference (1998), pp. 31.1–31.9
- 52.2 L.R. Newcome: *Unmanned Aviation, a Brief History of Unmanned Aerial Vehicles* (American Institute of Aeronautics and Astronautics, Reston 2004)
- 52.3 M.A. Garratt, J.S. Chahl: Vision-based terrain following for an unmanned rotorcraft, *J. Field Robotics* **25**(4/5), 284–301 (2008)
- 52.4 M. Garratt, H. Pota, A. Lambert, S. Eckersley-Maslin, C. Farabet: Visual tracking and lidar relative positioning for automated launch and recovery of an unmanned rotorcraft from ships at sea, *Naval Eng. J.* **121**(2), 99–110 (2009)
- 52.5 Vicon Motion Systems Ltd: <http://www.vicon.com/>
- 52.6 NaturalPoint Inc.: OptiTrack, <http://www.naturalpoint.com/optitrack/>
- 52.7 D. Mellinger, V. Kumar: Minimum snap trajectory generation and control for quadrotors, *Proc. Int. Conf. Robotics Autom. (ICRA)* (2011)
- 52.8 M. Hehn, R. D'Andrea: Quadcopter trajectory generation and control, *IFAC World Congress* (2011) pp. 1485–1491
- 52.9 M.W. Mueller, R. D'Andrea: A model predictive controller for quadcopter state interception, *European Control Conference* (2013) pp. 1383–1389
- 52.10 M.W. Mueller, M. Hehn, R. D'Andrea: A computationally efficient algorithm for state-to-state quadcopter trajectory generation and feasibility verification, *IEEE/RSJ International Conference on Intelligent Robots and Systems (IROS)* (2013) pp. 3480–3486
- 52.11 J. Thomas, J. Polin, K. Sreenath, V. Kumar: Avian-inspired grasping for quadrotor micro uavs, *ASME Int. Des. Eng. Tech. Conf. (IDETC)* (2013)
- 52.12 M. Turpin, N. Michael, V. Kumar: Trajectory design and control for aggressive formation flight with quadrotors, *Auton. Robots* **33**(1/2), 143–156 (2012)
- 52.13 S. Shen, Y. Mulgaonkar, N. Michael, V. Kumar: Vision-based state estimation for autonomous rotorcraft MAVs in complex environments, *Proc. IEEE Int. Conf. Robotics Autom.* (2013)
- 52.14 S. Shen, Y. Mulgaonkar, N. Michael, V. Kumar: Initialization-free monocular visual-inertial estimation with application to autonomous mavs, *Int. Symp. Exp. Robotics (ISER)* (2014)
- 52.15 T. Hamel, R. Mahony, R. Lozano, J. Ostrowski: Dynamic modelling and configuration stabilization for an X4-flyer, *Proc. Int. Fed. Autom. Control Symp. (IFAC)* (2002)
- 52.16 S. Bouabdallah, P. Murrieri, R. Siegwart: Design and control of an indoor micro quadrotor, *Proc. IEEE Int. Conf. Robotics Autom. (ICRA)*, Vol. 5 (2004) pp. 4393–4398
- 52.17 P.-J. Bristeau, P. Martin, E. Salaün, N. Petit: The role of propeller aerodynamics in the model of a quadrotor uav, *Proc. Eur. Control Conf.* (2009) pp. 683–688
- 52.18 H. Huang, G.M. Hoffmann, S.L. Waslander, C.J. Tomlin: Aerodynamics and control of autonomous quadrotor helicopters in aggressive maneuvering, *IEEE Int. Conf. Robotics Autom. (ICRA)* (2009) pp. 3277–3282
- 52.19 P. Pounds, R. Mahony, P. Corke: Modelling and control of a large quadrotor robot, *Control Eng. Pract.* **18**(7), 691–699 (2010)
- 52.20 M. Bangura, R. Mahony: Nonlinear dynamic modeling for high performance control of a quadrotor, *Australas. Conf. Robotics Autom.* (2012)
- 52.21 R. Mahony, V. Kumar, P. Corke: Multirotor aerial vehicles: Modeling, estimation, and control of quadrotor, *Robotics Autom. Mag.* **19**(3), 20–32 (2012)
- 52.22 R.W. Prouty: *Helicopter Performance, Stability and Control* (Krieger, Malabar 1995), reprint with additions

- 52.23 J.G. Leishman: *Principles of helicopter aerodynamics*, Cambridge Aerospace Series (Cambridge University Press, Cambridge 2000)
- 52.24 P. Martin, E. Salaun: The true role of accelerometer feedback in quadrotor control, *Proc. IEEE Int. Conf. Robotics Autom.* (2010) pp. 1623–1629
- 52.25 D. Abeywardena, S. Kodagoda, G. Dissanayake, R. Munasinghe: Improved state estimation in quadrotor mavs: A novel drift-free velocity estimator, *IEEE Robotics Autom. Mag.* **20**(4), 32–39 (2013)
- 52.26 R. Leishman, J. Macdonald, R.W. Beard, T.W. McLain: Quadrotors and accelerometers: State estimation with an improved dynamic model. *IEEE Control Syst. Mag.* **34**(1), 28–41 (2014)
- 52.27 A. Bramwell, G. Done, D. Balmford: *Bramwell's Helicopter Dynamics* (Butterworth Heinemann, Woburn 2001)
- 52.28 J.-L. Boiffier: *The Flight Dynamics: The Equations* (Wiley, Chichester 1998)
- 52.29 B.L. Stevens, F.L. Lewis: *Aircraft Control and Simulation*, 2nd edn. (Wiley, Hoboken 2003)
- 52.30 L.H. Carter, J.S. Shamma: Gain-scheduled bank-to-turn autopilot design using linear parameter varying transformations. *J. Guid. Control Dyn.* **19**(5), 1056–1063 (1996)
- 52.31 R.W. Beard, T.W. McLain: *Navigation, Guidance, and Control of Small Unmanned Aircraft* (Princeton University Press, Princeton 2012)
- 52.32 M.-D. Hua, T. Hamel, P. Morin, C. Samson: A control approach for thrust-propelled underactuated vehicles and its application to vtol drones, *IEEE Trans. Autom. Control* **54**(8), 1837–1853 (2009)
- 52.33 M. Bangura, H. Lim, H. Jin Kim, R. Mahony: Aerodynamic power control for multirotor aerial vehicles, *Proc. IEEE Int. Conf. Robotics Autom.* (2014), Paper MoB03.2.
- 52.34 P. Pounds, R. Mahony, P. Corke: Design of a static thruster for micro air vehicle rotorcraft, *ASCE J. Aerosp. Eng.* **22**(1), 85–94 (2009)
- 52.35 T. Lee, M. Leok, N.H. McClamroch: Geometric tracking control of a quadrotor UAV on  $se(3)$ , *Proc. IEEE Conf. Decis. Control* (2010)
- 52.36 M. Bangura, R. Mahony: Real-time model predictive control for quadrotors, *Proc. IFAC World Conf.* (2014)
- 52.37 H.K. Khalil: *Nonlinear Systems*, 2nd edn. (Prentice Hall, Upper Saddle River 1996)
- 52.38 D. Pucci: Flight dynamics and control in relation to stall, *IEEE Am. Control Conf. (ACC)* (2012) pp. 118–124
- 52.39 S. Devasia, D. Chen, B. Paden: Nonlinear inversion-based output tracking, *IEEE Trans. Autom. Control* **41**(7), 930–942 (1996)
- 52.40 J.-F. Magni, S. Bennani, J. Terlou: *Robust Flight Control: A Design Challenge*, Lecture Notes in Control and Information Sciences, Vol. 224 (Springer, Berlin, Heidelberg 1997)
- 52.41 E. Slatyer, R. Mahony, P. Corke: Terrain following using wide field optic flow, *Proc. Australas. Conf. Robotics Autom. (ACRA)* (2010)
- 52.42 A.A. Lambregts: Vertical fight path and speed control autopilot design using total energy principles, *Proc. AIAA Guid. Control Conf.* (1983) pp. 559–569
- 52.43 L.F. Faleiro, A.A. Lambregts: Analysis and tuning of a total energy control system control law using eigenstructure assignment, *Aerosp. Sci. Technol.* **3**(3), 127–140 (1999)
- 52.44 M.J. Van Nieuwstadt, R.M. Murray: Real-time trajectory generation for differentially flat systems, *Int. J. Robust Nonlinear Control* **8**, 995–1020 (1998)
- 52.45 D. Mellinger, N. Michael, V. Kumar: Trajectory generation and control for precise aggressive maneuvers with quadrotors, *Int. J. Robotics Res.* **31**, 664–674 (2012)
- 52.46 L.E. Dubins: On curves of minimal length with a constraint on average curvature, and with prescribed initial and terminal positions and tangents, *Am. J. Math.* **79**, 497–516 (1957)
- 52.47 G. Yang, V. Kapila: Optimal path planning for unmanned air vehicles with kinematic and tactical constraints, *Proc. IEEE Conf. Decis. Control* (2002) pp. 1301–1306
- 52.48 A. Rahmani, X.C. Ding, M. Egerstedt: Optimal motion primitives for multi-UAV convoy protection, *Proc. Int. Conf. Robotics Autom.* (2010) pp. 4469–4474
- 52.49 S. Hosak, D. Ghose: Optimal geometrical path in 3D with curvature constraint, *Proc. IEEE/RSJ Int. Conf. Intell. Robots Syst. (IROS)* (2010) pp. 113–118
- 52.50 H. Yu, R.W. Beard: A vision-based collision avoidance technique for micro air vehicles using local-level frame mapping and path planning, *Auton. Robots* **34**(1/2), 93–109 (2013)
- 52.51 H. Chitsaz, S.M. LaValle: Time-optimal paths for a Dubins airplane, *Proc. 46th IEEE Conf. Decis. Control* (2007) pp. 2379–2384
- 52.52 M. Owen, R.W. Beard, T.W. McLain: Implementing dubins airplane paths on fixed-wing UAVs. In: *Handbook of Unmanned Aerial Vehicles*, ed. by G.J. Vachtsevanos, K.P. Valavanis (Springer, Berlin, Heidelberg 2014) pp. 1677–1702
- 52.53 S. Park, J. Deyst, J.P. How: Performance and Lyapunov stability of a nonlinear path-following guidance method, *AIAA J. Guid. Control Dyn.* **30**(6), 1718–1728 (2007)
- 52.54 D.R. Nelson, D.B. Barber, T.W. McLain, R.W. Beard: Vector field path following for miniature air vehicles, *IEEE Trans. Robotics* **37**(3), 519–529 (2007)
- 52.55 D.A. Lawrence, E.W. Frew, W.J. Pisano: Lyapunov vector fields for autonomous unmanned aircraft flight control, *AIAA J. Guid. Control Dyn.* **31**(5), 1220–1229 (2008)
- 52.56 V.M. Goncalves, L.C.A. Pimenta, C.A. Maia, B.C.O. Durta, G.A.S. Pereira: Vector fields for robot navigation along time-varying curves in  $n$ -dimensions, *IEEE Trans. Robotics* **26**(4), 647–659 (2010)
- 52.57 A. Khosravian, J. Trumpf, R. Mahony, T. Hamel: Velocity aided attitude estimation on  $so(3)$  with sensor delay, *Proc. Conf. Decis. Control* (2014)
- 52.58 M. Euston, P. Coote, R. Mahony, J. Kim, T. Hamel: A complementary filter for attitude estimation of a fixed-wing UAV, *Proc. IEEE/RSJ Int. Conf. Intell. Robots Syst. (IROS)* (2008) pp. 340–345

- 52.59 R. Mahony, M. Euston, J. Kim, P. Coote, T. Hamel: A nonlinear observer for attitude estimation of a fixed-wing UAV without GPS measurements, *Trans. Inst. Meas. Control* **33**(6), 699–717 (2011)
- 52.60 R. Mahony, T. Hamel, J.-M. Pflimlin: Complementary filter design on the special orthogonal group  $SO(3)$ , *Proc. IEEE Conf. Decis. Control (CDC)* (2005) pp. 1477–1484
- 52.61 R. Mahony, T. Hamel, J.-M. Pflimlin: Non-linear complementary filters on the special orthogonal group, *IEEE Trans. Autom. Control* **53**(5), 1203–1218 (2008)
- 52.62 S. Bonnabel, P. Martin, P. Rouchon: Non-linear symmetry-preserving observers on lie groups, *IEEE Trans. Autom. Control* **54**(7), 1709–1713 (2009)
- 52.63 J. Macdonald, R. Leishman, R. Beard, T. McLain: Analysis of an improved imu-based observer for multirotor helicopters, *J. Intell. Robot. Syst.* **74**(3/4), 1049–1061 (2014)
- 52.64 D. Hughes: Uavs face hurdles in gaining access to civil airspace, *Aviation Week* (2007)
- 52.65 K.C. Wong, C. Bil, G. Gordon, P.W. Gibbens: *Study of the Unmanned Aerial Vehicle (UAV) Market in Australia*, Tech. Rep. (Aerospace Technology Forum Report, Sydney 1997)
- 52.66 R. Sugiura, N. Noguchi, K. Ishii, H. Terao: Development of remote sensing system using an unmanned helicopter, *J. Jap. Soc. Agricult. Mach.* **65**(1), 53–61 (2003)
- 52.67 R. Sugiura, T. Fukagawa, N. Noguchi, K. Ishii, Y. Shibata, K. Toriyama: Field information system using an agricultural helicopter towards precision farming, *IEEE/ASME Int. Conf. Adv. Intell. Mechatron.* (2003) pp. 1073–1078
- 52.68 K. Schutte, H. Sahli, D. Schrottmayer, F.J. Varas: Arc: A camcopter based mine field detection system, *5th Int. Airborne Remote Sens. Conf.* (2001)
- 52.69 S.E. Wright: Uavs in community police work, *AIAA Infotechs., Aerospace* (2005)